Contribution of carbonatite and recycled oceanic crust to petit-spot lavas on the western Pacific Plate

Kazuto Mikuni[1,2]*, Naoto Hirano[2,3], Shiki Machida[4], Hirochika Sumino[5], Norikatsu Akizawa[6], Akihiro Tamura[7], Tomoaki Morishita[7], Yasuhiro Kato[4,8,9]

[1] AIST, Geological Survey of Japan, Research Institute of Geology and Geoinformation, Central 7, 1-1-1, Higashi, Tsukuba, Ibaraki 305-8567, Japan.

[2] Graduate School of Science, Tohoku University, 6-3 Aramaki-Aoba, Aoba-ku, Sendai 980–8578, Japan.

[3] Center for Northeast Asian Studies, Tohoku University, 41 Kawauchi, Aoba-ku, Sendai 980–8576, Japan.

[4] Ocean Resources Research Center for Next Generation, Chiba Institution of Technology, 2-17-1 Tsudanuma, Narashino 275-0016, Japan.

[5] Research Center for Advanced Science and Technology, the University of Tokyo, 4-6-1 Komaba, Meguro-ku, Tokyo 153-8904, Japan

[6] Atmosphere and Ocean Research Institute, the University of Tokyo, 5-1-5, Kashiwanoha, Kashiwa 277-8564, Japan.

[7] Earth Science Course, Kanazawa University, Kakuma, Kanazawa 920-1192, Japan.

[8] Department of Systems Innovation, School of Engineering, The University of Tokyo, 7-3-1 Hongo, Bunkyo-ku, Tokyo 113-8656, Japan.

[9] Submarine Resources Research Center, Research Institute for Marine Resources Utilization, Japan Agency for Marine-Earth Science and Technology (JAMSTEC), 2-15 Natsushima-cho, Yokosuka, Kanagawa, 237-0061, Japan.

* *Correspondence to* Kazuto Mikuni (kazuto.mikuni @aist.go.jp)

Authors' e-mail addresses and ORCiD numbers

Kazuto Mikuni[1,2]*	kazuto.mikuni@aist.go.jp	0000-0001-6939-4333
Naoto Hirano[2,3]	nhirano@tohoku.ac.jp	0000-0003-0980-3929
Shiki Machida[4]	shiki.machida@p.chibakoudai.jp	0000-0002-1069-7214
Hirochika Sumino[5]	sumino@igcl.c.u-tokyo.ac.jp	0000-0002-4689-6231
Norikatsu Akizawa[6]	akizawa@g.ecc.u-tokyo.ac.jp	0000-0003-4210-1160
Akihiro Tamura[7]	aking826@gmail.com	0000-0002-9112-7976
Tomoaki Morishita[7]	moripta@gmail.com	0000-0002-8724-6868
Yasuhiro Kato[4,8,9]	ykato@sys.t.u-tokyo.ac.jp	0000-0002-5711-8304

40

Abstract

Petit-spot volcanoes, occurring due to plate flexure, have been reported globally. As the petit-spot melts ascend from the asthenosphere, they provide crucial information of the lithosphere–asthenosphere boundary. Herein, we examined the lava outcrops of six monogenetic volcanoes formed by petit-spot volcanism in the western Pacific. We then analyzed the $^{40}Ar/^{39}Ar$ ages, major and trace element compositions, and Sr, Nd, and Pb isotopic ratios of the petit-spot basalts. The $^{40}Ar/^{39}Ar$ ages of two monogenetic volcanoes were ca. 2.6 Ma (million years ago) and ca. 0 Ma. The isotopic compositions of the western Pacific petit-spot basalts suggest geochemically similar melting sources. They were likely derived from a mixture of high-μ (HIMU) mantle-like and enriched mantle (EM)-1-like components related to carbonatitic/carbonated materials and recycled crustal components. The characteristic trace element composition (i.e., Zr, Hf, and Ti depletions) of the western Pacific petit-spot magmas could be explained by the partial melting of ~5% crust-bearing garnet lherzolite with 10% carbonatite flux to a given mass of the source, as implied by a mass balance-based melting model. This result confirms the involvement of carbonatite melt and recycled crust in the source of petit-spot melts. It provides insights into the genesis of tectonic-induced volcanoes, including Hawaiian North Arch and Samoan petit-spot-like rejuvenated volcanoes, that have similar trace element composition to petit-spot basalts.

Short Summary

Plate tectonics theory is the motion of rocky plates (lithosphere) over ductile zones (asthenosphere). The causes of the lithosphere–asthenosphere boundary (LAB) are controversial; however, petit-spot volcanism supports the presence of melt at the LAB. We conducted geochemistry, geochronology, and geochemical modeling of petit-spot volcanoes on the western Pacific Plate, and the results suggested that carbonatite melt and recycled oceanic crust induced the partial melting at the LAB.

1 Introduction

Among the upper mantle-derived alkali basaltic lavas in oceanic settings, those on thicker plates away from the mid-ocean ridge, could be divided into plume-related and non-plume-related volcanoes. Plume-related North Arch and post-erosional (rejuvenated-stage) volcanoes have been reported in Hawaii and Samoa (Bianco et al., 2005; Bizimis et al., 2013; Clague and Frey, 1982; Clague and

76   Moore, 2002; Dixon et al., 2008; Frey et al., 2000; Garcia et al., 2016; Hart et al., 2004; Konter and

77   Jackson, 2012; Koppers et al., 2008; Reinhard et al., 2019; Yang et al., 2003). Nonplume-related

78   intraoceanic alkali volcanoes, known as petit-spot volcanoes, probably originate where nearby plate

79   subduction causes plate flexures and upwelling of asthenospheric magma (Hirano et al., 2006; Hirano

80   and Machida, 2022; Machida et al., 2015, 2017; Yamamoto et al., 2014, 2018, 2020). The occurrence

81   of petit-spot volcanisms supports the presence of melt at the lithosphere–asthenosphere boundary

82   (LAB) below the area at least.

83   The occurrence of melt in the uppermost asthenosphere could be attributed to small-scale

84   convection, the presence of hydrous or carbonatitic components, or the uplift of the lithosphere in

85   response to plate flexure; however, the possibility of such an occurrence remains ambiguous (e.g.,

86   Bianco et al., 2005; Hua et al., 2023; Korenaga, 2020). The presence of CO_2 and

87   carbonated/carbonatitic materials is a significant factor in the formation of alkaline, silica-

88   undersaturated melt in the upper mantle (Dasgupta and Hirschmann, 2006; Dasgupta et al., 2007,

89   2013; Kiseeva et al., 2013; Novella et al., 2014). Experimental studies have shown that the solidus of

90   carbonate-bearing peridotite is lower than that of CO_2-free peridotite (Falloon and Green, 1989. 1990;

91   Foley et al., 2009; Ghosh et al., 2009). Moreover, carbonatites and Si-undersaturated melts are

92   generated through the partial melting of CO_2-bearing or carbonated peridotite. The produced melts

93   can exhibit continuous chemical variations depending on pressure (i.e., depth). Carbonatitic melts are

94   produced in the deep asthenosphere (300–110 km), while carbonated or alkali silicate melts are

95   generated in the shallower upper mantle (from ~110 to ~75 or 60 km) (Keshav and Gudfinnsson, 2013;

96   Massuyeau et al., 2015, 2021). Primary carbonated silicate magma and evolved alkali basalts have

97   been simultaneously observed at the post-spreading ridge in the South China Sea (Zhang et al., 2017;

98   Zhong et al., 2021). The occurrence of Hawaiian rejuvenated volcanoes can be attributed to a

99   carbonatite-metasomatized source with or without silicate metasomatism (Borisova and Tilhac, 2021;

100   Dixon et al., 2008; Zhang et al., 2022).

101   Submarine petit-spot volcanoes on the subducting northwestern (NW) Pacific Plate may have

102   originated from carbonate-bearing materials and crustal components (pyroxenite/eclogite) based on

103   characteristic trace elements, enriched mantle (EM)-1-like Sr, Nd, and Pb isotopic, and relatively low

104   Mg isotopic compositions (Liu et al., 2020; Machida et al., 2009, 2015). Particularly, the depletion of

105   specific high-field-strength elements (HFSEs) (i.e., Zr, Hf, and Ti) and the abundance of CO_2 in petit-

106   spot basalts imply that their melting sources are related to carbonated materials (Hirano and Machida,

107   2022; Okumura and Hirano, 2013). The nature of the uppermost part of the asthenosphere beneath the

108   oldest Pacific Plate aged 160 Ma was characterized using the eruptive ages and geochemical properties

109   of six newly observed petit-spot volcanoes and lava outcrops. We verified the contribution of

110   carbonatitic components and crustal materials to the melting source of petit-spot volcanoes to

111   understand the nature of the underlying lithosphere–asthenosphere system and model the geodynamic

112 evolution of the region.

113

114 **2 Background**

115

116 Over the last 20 years, there has been an increase in the understanding of petit-spot volcanic

117 settings, providing valuable insights into the nature of the lithosphere–asthenosphere system,

118 particularly in the NW Pacific region (Hirano et al., 2006; Hirano and Machida, 2022). As other

119 implications, subducted petit-spot volcanic fields with geological disturbances on the seafloor play a

120 role in controlling the hypocentral regions of megathrust earthquakes (Fujiwara et al., 2007; Fujie et

121 al., 2020; Akizawa et al., 2022). Additionally, the vestige of hydrothermal activity due to petit-spot

122 magmatism has recently been reported (Azami et al., 2023).

123 Petit-spot melts emerging from the asthenosphere, which are unrelated to mantle plume, could

124 play a crucial role in clarifying the nature of the LAB (Hirano and Machida, 2022). Their

125 asthenospheric origin was supported by MORB-like noble-gas isotopic ratios, multi-phase saturation

126 experiment, and geochemistry (Hirano et al., 2006; Hirano and Machida, 2022; Machida et al., 2015,

127 2017; Yamamoto et al., 2018). The LAB is recognized as a discontinuous transition in seismic

128 velocities at the base of the lithosphere, and its causes are attributed to hydration, melting, and mineral

129 anisotropy with considerations for the unique characteristics in each tectonic setting (e.g., Rychert and

130 Shearer, 2009). The occurrence of petit-spot volcanoes confirms the existence of melt at the LAB

131 beneath the area at least (Hirano et al., 2006). Recently, similar volcanic activities have been observed

132 globally, including in Java (Sunda) Trench, Tonga Trench, Chile Trench, Mariana Trench, Costa Rica,

133 North American Basin and Range, and the southern offshore of Greenland, implying the universal

134 occurrence of petit-spot and similar magmatisms (Axen et al., 2018; Buchs et al., 2013; Falloon et al.,

135 2022; Hirano et al., 2013, 2016, 2019; Reinhard et al., 2019; Taneja et al., 2016; Uenzelmann-Neben

136 et al., 2012; Yamamoto et al., 2018, 2020; Zhang et al., 2019). Although the question of whether the

137 LAB discontinuity is due to the differences in the physical properties of minerals (e.g., Hirth and

138 Kohlstedt, 1996; Kang and Karato, 2023; Karato and Jung, 1998; Katsura and Fei, 2021; Stixrude and

139 Lithgow-Bertelloni, 2005; Wang et al., 2006) or the presence of partial melts remains open (e.g.,

140 Audhkhasi and Singh, 2022; Chantel et al., 2016; Conrad et al., 2011; Debayle et al., 2020; Herath et

141 al., 2022; Hua et al., 2023; Kawakatsu et al., 2009; Mierdel et al., 2007; Sakamaki et al., 2013; Yoshino

142 et al., 2006), the occurrence of petit-spot volcanism indicates the partial melting of the asthenospheric

143 mantle in the region because they erupted on the seafloor without hotspot and ridge activities (Hirano

144 et al., 2006; Hirano and Machida, 2022; Machida et al., 2015, 2017; Yamamoto et al., 2014, 2018,

145 2020).

146 The petit-spot volcanic province on the abyssal plain of the western Pacific is surrounded by

147 Cretaceous seamounts and oceanic islands of the Western Pacific Seamount Province (Koppers et al.,

148   2003) and is located ~100 km southeast of the Minamitorishima (Marcus) Island (Fig. 1a). The study

149   area corresponds to the oldest portion of the Pacific Plate, aged at 160 Ma, and the foot of the outer-

150   rise bulge related to the Mariana subduction system (Hirano et al., 2019; Fig. 1b). Despite several

151   seamounts crosscutting, subduction-related fore-bulge in front of the Mariana Trench was detected in

152   satellite gravity maps and has been numerically modeled (Bellas et al., 2022; Hirano et al., 2019;

153   Zhang et al., 2014, 2020). Petrography, geochemistry, and geochronology of petit-spot basalts and

154   zircons in peperites collected from a knoll suggest that petit-spot magmas in this region ascend from

155   the asthenosphere along the concavely flexed plate in response to subduction into the Mariana Trench

156   at younger than ~3 Ma (Yamamoto et al., 2018; Hirano et al., 2019). Below the study area, a low

157   seismic velocity zone is observed under the lithosphere (Li et al., 2019; Fig. 1c). Notwithstanding the

158   low-velocity anomalies crosscutting the lower mantle (Fig. 1c), no active hotspots (i.e., heat supplies)

159   have been reported around the western Pacific petit-spot province , which is surrounded by Cretaceous

160   Wake seamount chains including Minamitorishima Island and Paleogene intraplate volcanoes

161   (Koppers et al., 2003; Aftabuzzaman et al., 2021; Hirano et al., 2021). Other petit-spot lava outcrops

162   were observed in a volcanic cluster during three research cruises using the research vessel (RV)

163   *Yokosuka* (YK16-01, YK18-08, and YK19-05S) with five dives using the submersible, *Shinkai* 6500

164   (6K#1466, 6K#1521, 6K#1522, 6K#1542, and 6K#1544; Fig. 2); and here, fresh basalts were collected.

165   Information related to the sampling point, depth, and thickness of palagonite rind and manganese-crust

166   as well as the age of the western Pacific petit-spot basalts are provided in Table 1.
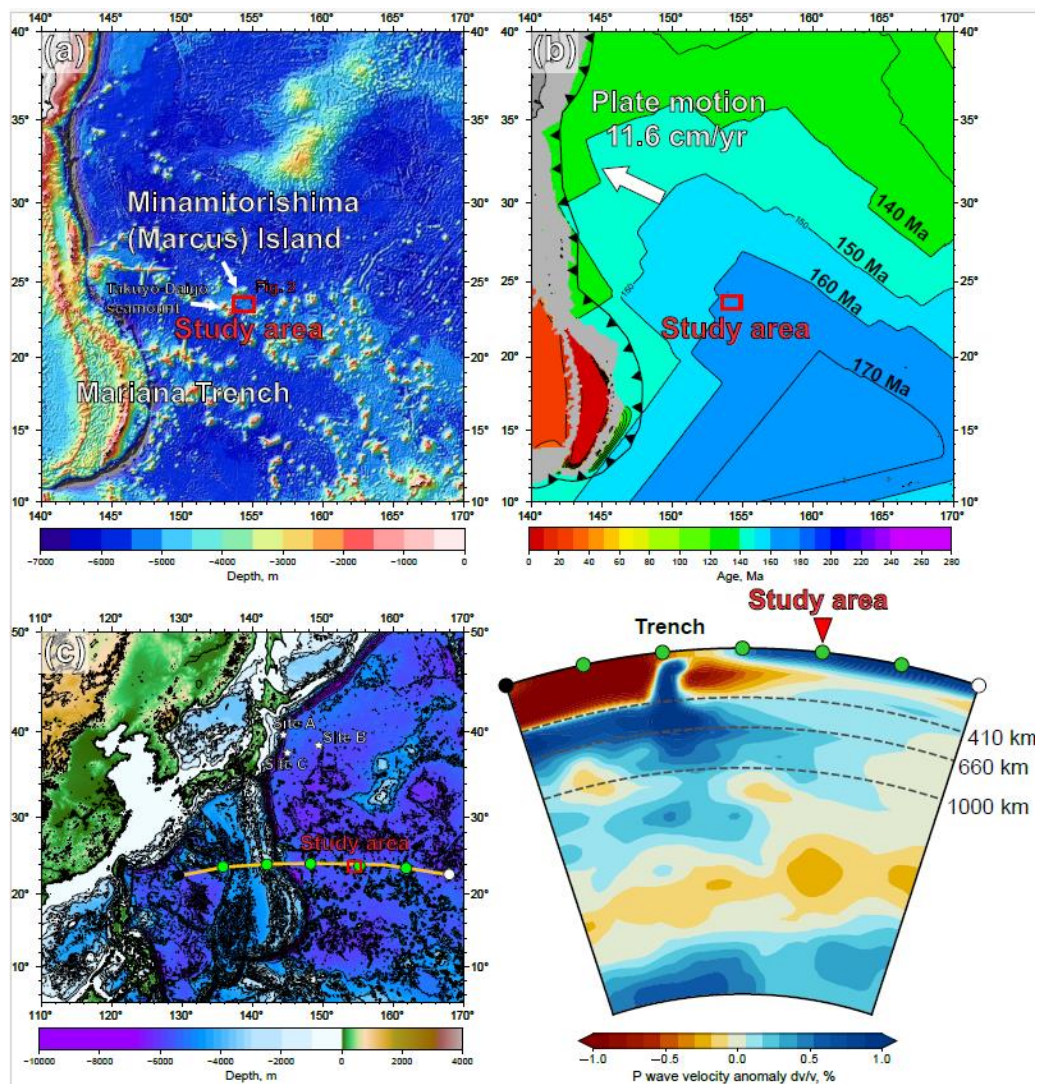
Fig. 1. Geological and geophysical information of the study area. (a) Bathymetry of the western Pacific near the Mariana Trench. The red box shows the study area to the southeast of Minamitorishima (Marcus) Island (Fig. 2). The bathymetric data are adopted from ETOPO1 (NOAA National Geophysical Data Center; http://www.ngdc.noaa.gov/). (b) Seafloor age map of the same area as (a). This study area is on a 160–170 Ma Pacific Plate, called the Jurassic Quiet Zone (JQZ) (Tivey et al. 2006). The present absolute motion of the Pacific Plate and the seafloor age are derived from studies by Gripp and Gordon (1990) and Müller et al. (2008), respectively. (c) The cross-section P-wave tomography beneath the thick yellow line including the study area on the ETOPO1 bathymetry map (left). The bathymetric images were drawn using the Generic Mapping Tool (GMT6: Wessel et al., 2019). The tomographic image (right) was drawn using the SubMachine (Hosseini et al., 2018; http://www.earth.ox.ac.uk/~smachine/cgi/index.php) on applying the data of Lu et al. (2019).

Table. 1
Information of the collected western Pacific petit-spot basalts

Cruise	Dive	Sample name	Latitude (N)	Longitude (E)	Depth, m	Palagonite rind, mm [1]	Manganese crust, mm [1]	Ar-Ar age, Ma
YK16-01	6K#1466	R3-001	23° 19.1009	154° 15.0950	5453	4.45	7.155	
		R3-04	23° 19.1009	154° 15.0950	5453	3.005	5.805	
		R6-001	23° 19.4475	154° 15.0367	5300	6.61	5.205	2.56±0.34
		R7-001	23° 19.4713	154° 15.0000	5267	5.54	4.31	
		R7-003	23° 19.4713	154° 15.0000	5267	-	–	
YK18-08	6K#1521	R04	23° 5.0880	154° 23.7360	5546	1.045	5.935	
		R05	23° 5.0880	154° 23.7360	5546	-	5.625	
	6K#1522	R01	23° 27.6420	153° 58.3140	5300	6.015	5.78	-0.11±0.23[2]
		R02	23° 27.6420	153° 58.3140	5300	4.505	2.66	
		R03	23° 27.6420	153° 58.3140	5300	5.44	4.04	
		R05	23° 27.6360	153° 58.3080	5294	2.92	4.785	
		R12	23° 27.4920	153° 58.0620	5189	6.05	5.56	
		R13	23° 27.4920	153° 58.0620	5189	4.545	5.895	
		R14	23° 27.3540	153° 57.8160	5303	2.04	5.475	
		R16	23° 27.4680	153° 57.1200	5182	3.825	3.845	
		R17	23° 27.4680	153° 57.1200	5182	5.19	5.67	
YK19-05S	6K#1542	R03	23° 44.1926	154° 45.6900	5359	3.43	4.26	
		R05	23° 44.1926	154° 45.6900	5359	3.245	4.355	
		R06	23° 44.7064	154° 44.1200	5190	-	-	
		R09	23° 44.7064	154° 44.1200	5190	-	-	
	6K#1544	R04	23° 43.9555	154° 49.4277	5488	4.39	4.955	
		R05	23° 43.9555	154° 49.4277	5488	2.965	4.97	
		R06	23° 43.9555	154° 49.4277	5488	3.425	5.82	

[1]: The samples which have no data of palagonite and/or Mn-crust thickness are due to the lack of them or crumbled.

[2]: This is a reference value due to the lack of radiogenic ^{40}Ar in this sample.
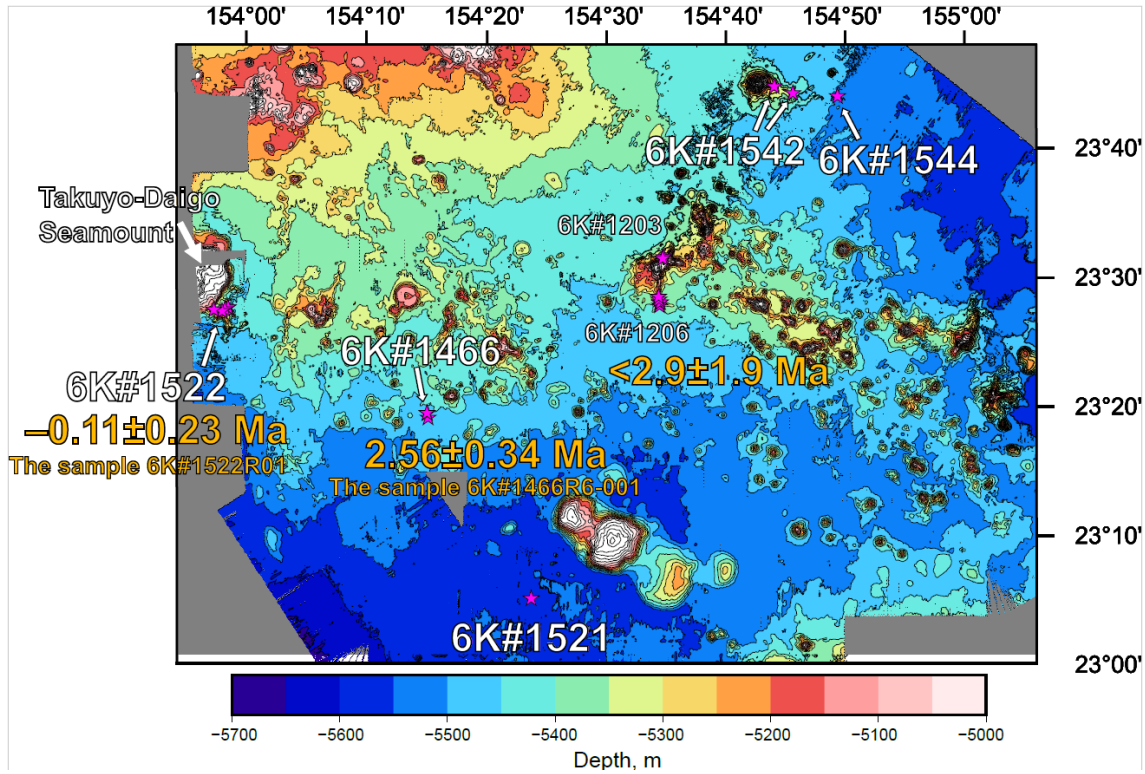
Fig. 2. Detailed bathymetry of the study area. The onboard multibeam data were surveyed during the YK10-05 and the YK18-08 cruises by the Japan Agency for Marine-Earth Science and Technology (JAMSTEC). The petit-spot knolls and outcrops were investigated during several dives as 6K#1466, 6K#1521, 6K#1522, 6K#1542, and 6K#1544. The pink-colored stars represent the sampling points. The age information was obtained in the present study and Hirano et al. (2019). The bathymetric image was drawn using the GMT (Wessel et al., 2019).

3 Field observations, sample locations, and petrography

Here, the eruption sites of monogenetic volcanoes or lava outcrops are approximately aligned with each dive site numbered 6K#1466, #1521, #1522, #1542, and #1544 conducted using the *Shinkai* 6500. The 6K#1466 dive was conducted at two types of monogenetic volcanoes, categorized as glassy type (R3) and crystalline and vesicular type (R6 and R7) based on the geochemical and petrographic descriptions and occurrence of basaltic samples.

3.1 YK16-01 cruise and 6K#1466 dive

During the YK16-01 cruise, a small conical knoll (ca. 0.04 km^3) was investigated by a submersible dive, 6K#1466 (Figs. 2 and 3a). The lava flows, which were observed in a hollow lava tube resulting in sediment-rolling/disturbing eruption, were located ~600 m south of the top of the knoll, featuring extremely fresh and glassy samples (6K#1466R3-001 and R3-004 basalts) (Fig. 3a). Vesicular pillow basalts were collected on the western slope of the knoll (samples 6K#1466R6-001, R7-001, and R7-003; Fig. 3a). While the strong acoustic reflection could not entirely distinguish the petit-spot lava fields in ferromanganese nodule fields, the 6K#1466 dive revealed lava outcrops using a sub-bottom profiler (SBP) and a multinarrow-beam echo sounder (MBES). Specifically, the petit-spot lava field, as an acoustically opaque layer, exhibited a vigorous backscattering intensity in the MBES, along with the distributions of the basement and sediment layers in the SBP.

The 6K#1466R3-001 and R3-004 samples were extremely fresh glassy basalts. The samples exhibited similar petrographic features (Fig. 3a). These samples were enveloped by a 3.0–4.5-mm-thick palagonite layer (hydrated quenched glass), with their outermost parts being surrounded by a 5.8–7.2-mm-thick ferromanganese crust (Fig. 3a). They were less vesicular (<3 vol.%) and were dominantly composed of basaltic glass, euhedral–subhedral olivine microphenocrysts (~100–500 μm in size), ferrotitanium oxide (<50 μm in size), and minor plagioclase (~500 μm in size) (Fig. 3a). No secondary phases such as clay minerals were observed.

The 6K#1466R6-001, R7-001, and R7-003 basalts, which were covered with a 4.3–5.2-mm-thick ferromanganese crust over 5.5–6.6-mm-thick palagonite rinds, exhibited high vesicularity (20–40 vol.%) (Fig. 3a). Mikuni et al. (2022) reported certain pyroxene-dominated xenocrysts and peridotite xenoliths. The basaltic groundmass was characterized by needle-shaped clinopyroxene (50–400 μm in size), subhedral olivine partly with aureoles of iddingsite (up to 100 μm in size), ferrotitanium oxide, minor spinel (up to 10 μm in size), glass, and crystallite, notably without remarkable phenocrysts (Fig. 3a). The photomicrograph of R6-001 is shown in Fig. 3a.

3.2 YK18-08 cruise and 6K#1521 and 6K#1522 dives

226

Two submersible dives (6K#1521 and #1522) were conducted during the YK18-08 cruise to investigate petit-spot volcanoes. During the 6K#1521 dive, a small lava outcrop was identified in the abyssal plain by tracing a strong acoustic reflection, which was expected to originate from intrusive rock bodies, in the sedimentary layer detected by deep-sea SBP equipped on the *Shinkai* 6500. The strong reflective surface gradually became shallow during the navigation, revealing the small lava outcrop (Figs. 2 and 3b). Fresh and massive (nonvesicular) basalts were collected from this outcrop (samples 6K#1521R04 and R05; Fig. 3b). The samples obtained from the 6K#1522 dive at a seamount exhibited highly irregular shapes, and massive lava flows, pillows, and lava breccia were observed (Fig. 3c). All the samples were fresh vesicular basalts (6K#1522R01, R02, R05, R12, R13, R16, and R17; Fig. 3c).

The fresh, massive, and nonvesicular basalts were collected during the 6K#1521 dive (R04 and R05) comprised euhedral olivine microphenocrysts (150–400 μm in size), two types of ferrotitanium oxide (50–150 μm in size), and crystallite (Fig. 2b). Secondary phases were not observed. They were covered with a 5.6–5.9-mm-thick ferromanganese crust and a ~1.0-mm-thick palagonite rind (Fig. 3b), however, R05 did not have palagonite rinds. The photomicrograph of R04 is shown in Fig. 3b.

The seven fresh basalts collected during the 6K#1522 dive (6K#1522R01, R02, R05, R12, R13, R16, and R17), exhibited high vesicularity (20–40 vol.%) with 2.9–6.0-mm-thick palagonite rinds covered with 2.7–5.9-mm-thick ferromanganese crusts (Fig. 3c). Euhedral–subhedral olivine microphenocrysts (glomeroporphyritic, 30–200 μm in size), radial–needle-shaped clinopyroxene, iddingsite (<200 μm in size), spinel, and glass with minor xenocrystic olivines were observed (Fig. 3c). The photomicrograph of R01 is shown in Fig. 3c.

3.3 YK19-05S cruise and 6K#1542 and 6K#1544 dives

A petit-spot knoll and associated lava flows were investigated by the 6K#1542 and #1544 dives during the YK19-05S cruise (Fig. 2). During the 6K#1542 dive, geological survey and rock sampling were conducted from two points on the eastern slope of the knoll (Figs. 2 and 3d). The 6K#1542R03 and R05 basalts were collected from the lava-breccia field covered with a thin ferromanganese crust (Fig. 3d). Additionally, samples R06 and R09 were obtained from the lobate-surface lava between tubular lavas closer to the summit than R03 and R05 (Fig. 3d).
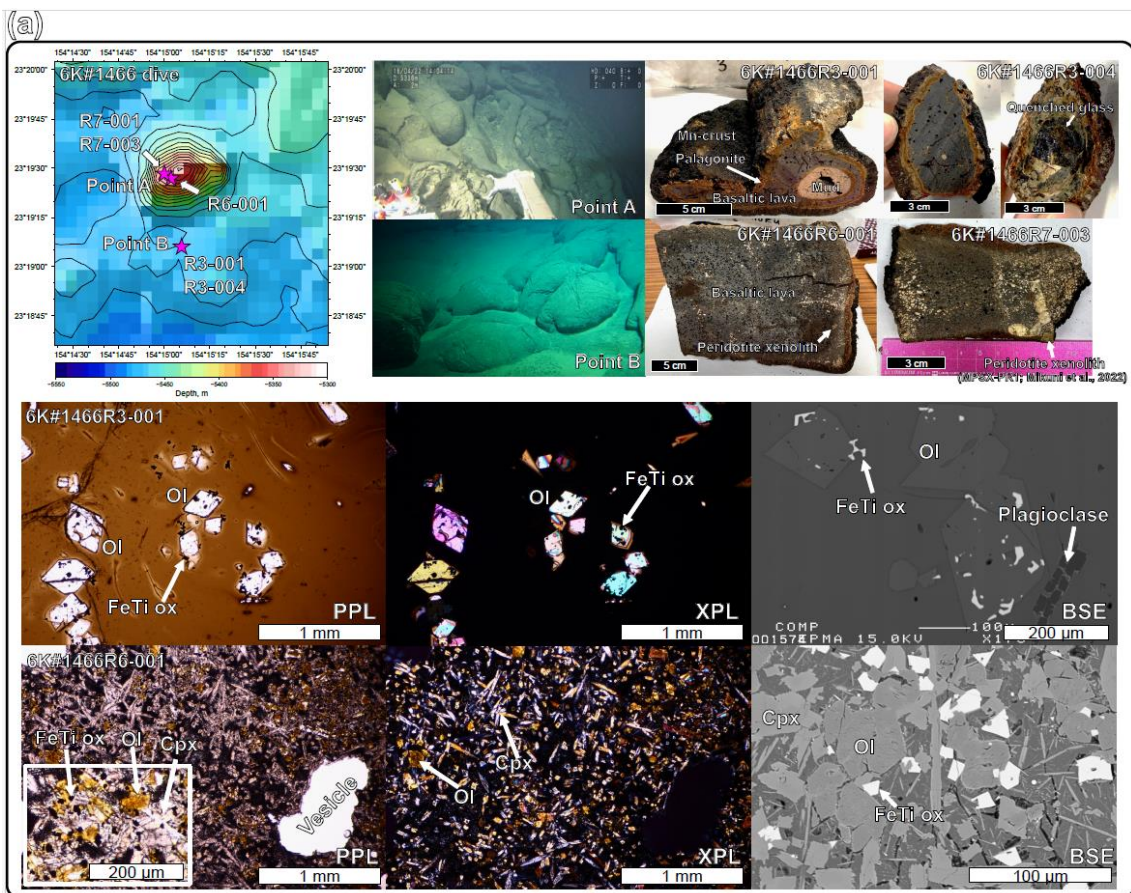
High-resolution (one-meter scale) bathymetric mapping was successfully conducted during the 6K#1544 dive, which can contribute to future oceanographic investigations using a human-occupied vehicle (Kaneko et al., 2022). Several mounds, 10–20 m in height and a few hundred meters in diameter, were recognized during this acoustic survey (Fig. 3d). We observed these mounds and collected samples from outcrops during the second half of the dive. Furthermore, pillow lavas, tumuli,

262 and lava breccias were observed, and basaltic samples (6K#1544R04, R05, and R06) were collected
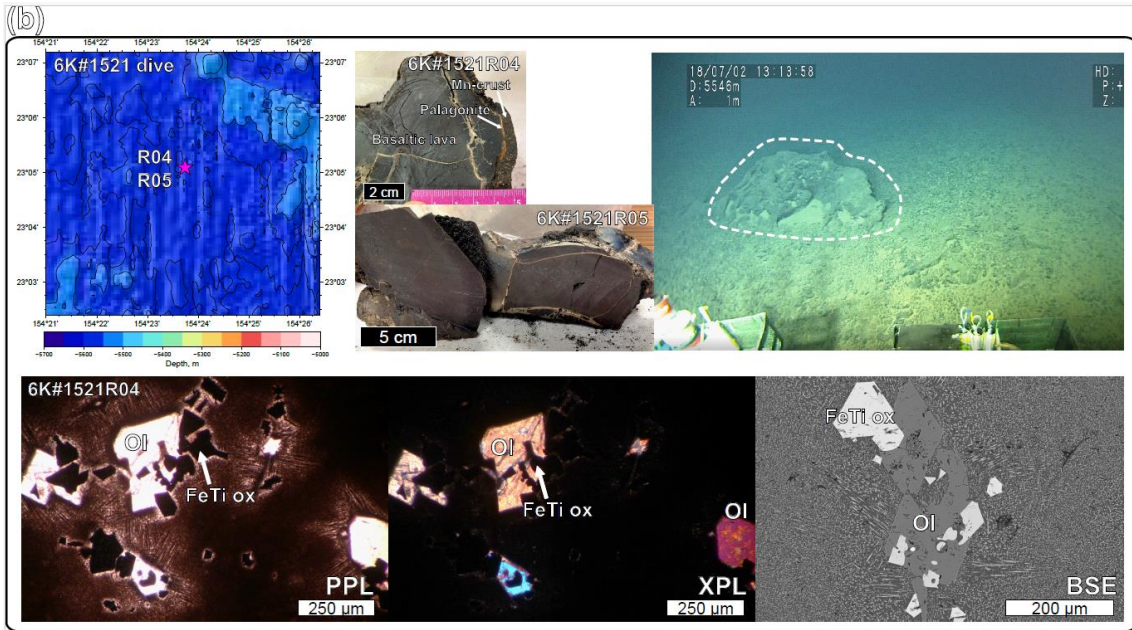263 (Fig. 3d).

264   Four vesicular basalts (10–30 vol.% vesicularity; 6K#1542R03, R05, R06, and R09) were
265 covered with 4.3–4.4-mm-thick ferromanganese crusts. The outer palagonitic rinds were 3.2–3.4-mm-
266 thick (Fig. 3d). Euhedral–subhedral olivine microlites (up to sizes of 300 μm) and microphenocrysts
267 were glomeroporphyritic (Fig. 3d). The groundmass was dominated by needled dendritic
268 clinopyroxenes (~100 μm in size), along with olivine, spinel, glass, and xenocrystic olivine megacrysts.
269 The photomicrograph of R06 is shown in Fig. 3d.

270   Basaltic samples from the 6K#1544 dive (6K#1544R04, R05, and R06) were covered with
271 ferromanganese crust (5.0–5.8-mm thick) over palagonitic rinds (3.4–4.4-mm thick). All the samples
272 exhibited high vesicularity in the range of 20–35 vol.% (Fig. 3d). They comprised olivine
273 microphenocrysts (30–250 μm in size, euhedral–subhedral or columnar), clinopyroxene (<100 μm,
274 needled, columnar, radial or dendritic shape), spinel, and glass without secondary phases (Fig. 3d).
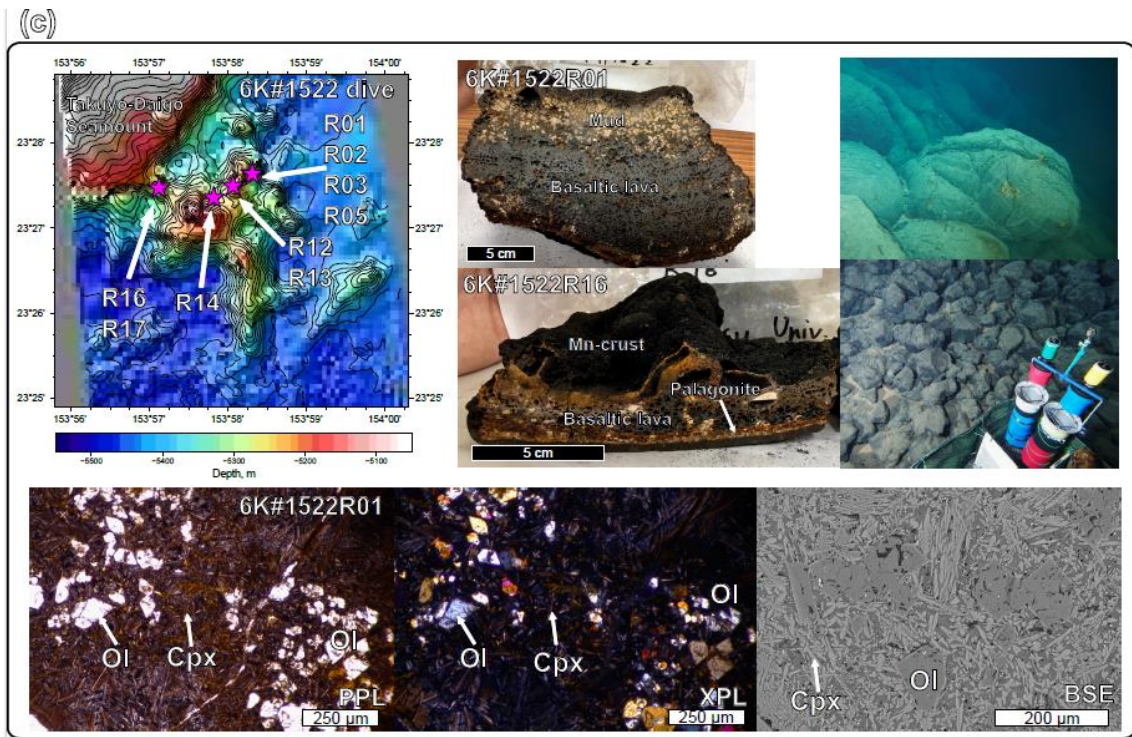
275   The photomicrograph of R04 is shown in Fig. 3d. During macroscopic observations, practically
276 all the basalts from the 6K#1542 and 6K#1544 dives exhibited similar vesicularity and freshness.
277 Their geochemical features were also similar to each other and are described in Sect. 5-1 and 5-2.

278

279

(b)

6K#1521 dive

R04
R05

6K#1521R04
Mn-crust
Palagonite
Basaltic lava
2 cm

6K#1521R05
5 cm

18/07/02 13:13:58
D:5546m
A: 1m

6K#1521R04

Ol
FeTi ox
PPL
250 µm

Ol
FeTi ox
XPL
Ol
250 µm

FeTi ox
Ol
BSE
200 µm

280

(c)

Takuyo-Daigo Seamount

6K#1522 dive

R01
R02
R03
R05
R12
R13
R16
R14
R17

6K#1522R01
Mud
Basaltic lava
5 cm

6K#1522R16
Mn-crust
Palagonite
Basaltic lava
5 cm

6K#1522R01

Ol
Cpx
Ol
PPL
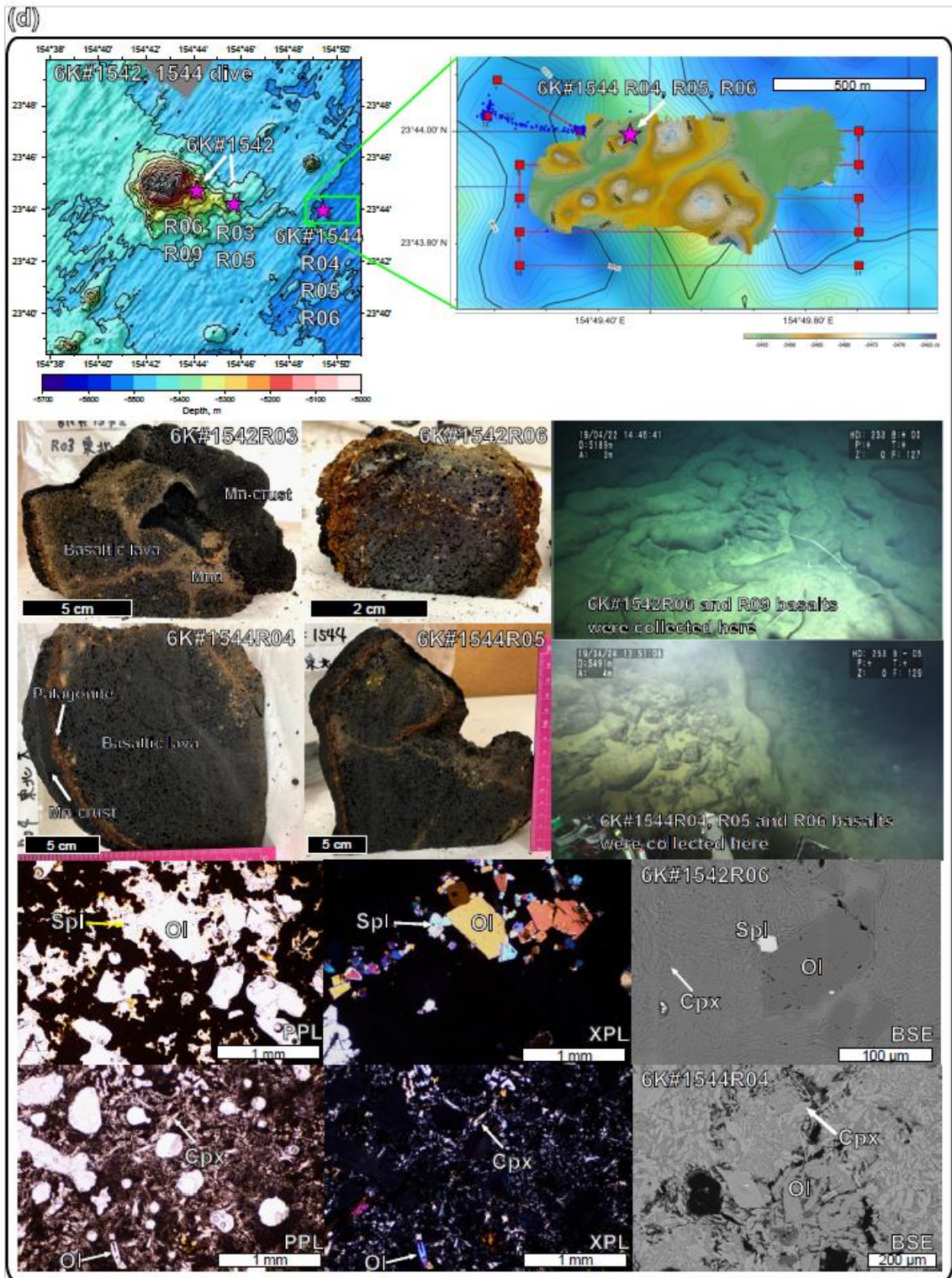250 µm

Ol
Ol
Cpx
XPL
250 µm

Ol
Cpx
BSE
200 µm

281

Fig. 3. Bathymetric map with photos of the outcrop, the collected samples, and their photomicrographs with detailed bathymetry of the sampling points. (a) The 6K#1466, (b) 6K#1521, (c) 6K#1522, and (d) 6K#1542 and 6K#1544 dives using the *Shinkai* 6500 by JAMSTEC. The 1-m gridded bathymetry of the 6K#1544 dive is shown in (d), obtained using an MBES equipped with the *Shinkai* 6500 over a 100-m resolution map

287   obtained using the surface ship, R/V *Yokosuka* (Kaneko et al., 2022). The photomicrographs of

288   representative samples are shown for plane-polarized light (PPL), cross-polarized light (XPL), and

289   backscatter electron (BSE). Ol, olivine; Cpx, clinopyroxene; Mgt, magnetite; Spl, spinel. The bathymetric

290   images were drawn using the GMT (Wessel et al., 2019). Photos of seafloor lava-outcrops were provided

291   by the cruise report of YK16-01, YK18-08, and YK19-05S cruises in the Data and Sample Research

292   System for Whole Cruise Information by JAMSTEC (http://www.godac.jamstec.go.jp/darwin/).

293

294

295 **4. Analytical methods**

296

297 **4.1 Major and trace element analysis of volcanic glass, mineral, and whole-rock**

298

299   Major element compositions of glasses and minerals were determined using an electron probe

300 micro analyzer (EPMA). JXA-8900R at Atmosphere and Ocean Research Institute (AORI), the

301 University of Tokyo was used for glass analysis and JXA-iHP200F at GSJ, AIST was used for mineral

302 analysis. The analyses were performed using an accelerating voltage of 15 kV, a beam current of 12

303 nA, and a beam diameter of 10 μm for glass and 2 μm for mineral. A peak counting time of 20 s and

304 a background counting time of 10 s were used, except for Ni, for which a peak counting time of 30 s

305 and a background counting time of 15 s. For Na analysis of glass, the peak counting time was 5 s and

306 the background counting time was 2 s. Natural and synthetic minerals were used as standards, and data

307 were corrected using a ZAF online correction program (Akizawa et al., 2021). Major element

308 composition of glass was determined by the mean value of 10 analytical points.

309   Trace element compositions of minerals were determined using a laser ablation-inductively

310 coupled plasma-mass spectrometry (LA-ICP-MS; New Wave Research UP-213 and Agilent 7500s)

311 at Kanazawa University. The Nd: YAG deep UV (ultraviolet) laser's wavelength is 213 nm. The

312 analyses were conducted with 100 μm spot size. A repetition frequency of 6 Hz and a laser energy

313 density of 8 J cm^{-2} were used. NIST612 glass (distributed by National Institute of Standards and

314 Technology) was employed for calibration, using the preferred values of Pearce et al. (1997). Data

315 reduction was undertaken with ^{29}Si as the initial standard, and SiO$_2$ concentrations were obtained by

316 an electron microprobe analysis (Longerich et al., 1996). BCR-2G (distributed by the United States

317 Geological Survey) was used as a secondary standard to assess the precision of each analytical

318 session (Jochum and Nohl, 2008).

319   Whole-rock major and trace element compositions of rock samples were analyzed by Activation

320 Laboratories Ltd., Canada, using Code 4Lithoresearch Lithogeochemistry and ultratrace5 Exploration

321 Geochemistry Package. The former package uses lithium metaborate/tetraborate fusion with

322 inductively coupled plasma optical emission spectrometry (FUS-ICP-OES) and inductively coupled

plasma mass spectroscopy (FUS-ICP-MS) for the major and trace element analyses, respectively. The latter package uses inductively coupled plasma optical emission spectrometry (ICP-OES) and inductively coupled plasma mass spectroscopy (ICP-MS) for the major and trace element analyses, respectively.

4.2 Sr, Nd, and Pb isotope analysis

4.2.1 Acid leaching

Acid leaching was conducted for the selected basaltic samples on the basis of the procedure of Weis and Frey (1991, 1996) as follows: [1] About 0.3–0.4 or 0.6 g of rock powder is weighed into an acid-washed 15 mL Teflon vial (Savilex®). [2] 10 or 12 mL of 6N (N: normality) HCl were added, and then heated at 80°C for 20–30 min. [3] After heating, the suspension is ultra-sonicated in 60°C water for 20 min. [4] The supernatant is decanted. Steps [2] to [4] were repeated more than 4 times (up to 6 times) until the supernatant become clear or pale yellow to colorless. [5] TAMAPURE-AA Ultrapure water (Tama Chemicals; Co., Ltd.), which includes a lower Pb blank than milli-Q H_2O, were added instead of 6N HCl, and the suspension is ultra-sonicated for 20 min. This step is conducted twice. [6] The leached rock powder is dried on a hot plate at 120°C. [7] After cooling, the powder is weighed.

4.2.2 Extraction of Pb, Sr, and Nd

The extraction of Pb, Sr, and Nd was performed following the procedures of Tanimizu and Ishikawa (2006) and Machida et al. (2009). First, from ~50 to ~100 mg of rock powder was weighted in a 7 mL Teflon vial (designated as "vial A"), and digested using mixed acid composed of HF and HBr. The separation was conducted by cation exchange resin (AG-1X8; Bio-Rad Laboratories Inc.) on the basis of procedures described in Tanimizu and ishikawa (2006). All fractions from the first and second supernatant loading (0.5 M HBr) to the elution of other elements (mixed acid composed of 0.25 M HBr and 0.5 M HNO_3) were collected in another 7 mL Teflon vial (designated as "vial B") for Sr and Nd separation. Finally, Pb was extracted by 1 mL of 1M HNO_3 in another 7 mL Teflon vial (designated as "vial C"). The procedural blanks for Pb totaled less than 23 pg.

The Sr and Nd-bearing solution in the vial B was transferred into the vial A containing residues of digested samples. 2 mL of $HClO_4$ and 2 mL HNO_3 was further added to the vial A, and the residue was dissolved at 110 °C. Both Sr and Nd were separated by column with a cation exchange resin (AG50W-8X; Bio-Rad Laboratories Inc.) and a Ln resin (Eichrom Tech- nologies Inc.) on the basis of procedures described in Machida et al. (2009). The separated Sr and Nd were further purified by column separation with a cation exchange resin. The total procedural blanks for Sr and Nd were less

359   than 100 pg.

360

361   **4.2.3 Analytical procedure**

362

363   Pb isotopic ratios were obtained using the multi-collector ICP-MS (MC-ICP-MS; Neptune plus,

364   Thermo Fisher Scientific), with nine Faraday collectors, at Chiba Institute of Technology (CIT), Japan.

365   The NIST SRM-981 Pb standard was also analyzed and yielded the average values of $^{206}Pb/^{204}Pb =$

366   16.9303 ± 0.0005, $^{207}Pb/^{204}Pb = 15.4828 \pm 0.0006$, and $^{208}Pb/^{204}Pb = 36.6710 \pm 0.0016$. These

367   correspond to previous values determined using MC-ICP-MS with Tl normalization, but they were

368   slightly lower than values determined by TIMS in Tanimizu and Ishikawa (2006) from the $^{207}Pb–^{204}Pb$

369   double-spike. Reproducibility was monitored by an analyses of the JB-2 GSJ standard, and the

370   obtained values were $^{206}Pb/^{204}Pb = 18.3326 \pm 0.0005$, $^{207}Pb/^{204}Pb = 15.5453 \pm 0.0006$, and $^{208}Pb/^{204}Pb$

371    $= 38.2240 \pm 0.0017$.

372   Sr and Nd isotopic analyses for powdered rocks and glasses were conducted using the thermal

373   ionization mass spectrometry (TIMS; Triton XT, Thermo Fisher Scientific) with nine Faraday

374   collectors, at CIT. 1.5 µL of 2.5M HCl and 0.5M HNO_3 was used for loading of separated Sr and Nd

375   of sample on the single and double Re-filament, respectively. The measured isotopic ratios were

376   corrected for instrumental fractionation by adopting the $^{86}Sr/^{85}Sr$ value to be 0.1194 and that of

377    $^{146}Nd/^{144}Nd$ to be 0.7219. The average value for the NIST SRM-987 Sr standard was 0.710239

378   ±0.000005 (2σ, n =2), and that for the GSJ JNdi-1 Nd standard was 0.512103 ±0.000005 (2σ, n =2).

379   They agree well with values from the literature for the NIST SRM-987 ($^{87}Sr/^{86}Sr = 0.710252–$

380   0.710256; Weis et al., 2006) and JNdi-1 ($^{143}Nd/^{144}Nd = 0.512101$; Wakaki et al., 2007). Consequently,

381   we did not correct the values of the unknowns for offsets between the measurements and the values

382   for the Sr and Nd standards.

383

384   **4.3 $^{40}Ar/^{39}Ar$ dating**

385

386   Samples for $^{40}Ar/^{39}Ar$ dating were prepared by separating crystalline groundmass after crushing

387   them to sizes between 100 and 500 µm. The separated groundmass samples were leached by HNO_3 (1

388   mol/L) for one hour to remove clays and altered materials. All samples were wrapped in aluminum

389   foil along with JG-1 biotite (Iwata, 1998), K_2SO_4, and CaF_2 flux monitors. Any amorphous (e.g.,

390   quenched glass) was removed because ^{39}Ar may move from one phase to another in a process known

391   as "recoil." This can create a disturbed age spectrum when ^{39}Ar is produced from ^{39}K in amorphous

392   material through interaction with fast neutrons during irradiation of the sample. Samples were

393   irradiated for 6.6 days in the Kyoto University Research Reactor (KUR), Kyoto University. Argon

394   extraction and isotopic analyses were undertaken at the Graduate School of Arts and Sciences, the

395   University of Tokyo. The sample gases were extracted by incremental heating of 10 or 11 steps

396   between 600°C and 1500°C. The analytical methods used are the same as those used by Ebisawa et al.

397   (2004) and Kobayashi et al. (2021).

398

399   **5 Results**

400

401   To describe the geochemical and chronological results, each sample group was denoted by its

402   dive number, e.g., the sample group obtained from the 6K#1521 dive was labeled "1521 samples or

403   basalts". The basalts from the 6K#1466 dive were divided into two groups for R3 (collected from the

404   seafloor south of the knoll) and R6–R7 (sampled on the knoll) based on their geographical,

405   petrological, and compositional differences. The mineral compositions of each petit-spot basalt are

406   shown in Fig. S1 and Table S1, S2 and S3.

407

408   **5.1 Major and trace element compositions**

409

410   The major and trace element compositions for the whole rock and glass of the petit-spot basalts

411   are listed in Table 2 and 3, respectively. The basalt compositions for a petit-spot knoll were reported

412   by Hirano et al. (2019) (expressed as "1203, 1206" in each figure). The data are discussed along with

413   the reported NW Pacific petit-spots (Hirano and Machida, 2022). Using a total alkali vs. silica (TAS)

414   diagram, virtually all the samples were classified as alkalic rocks, but the 1542 and 1544 basalts were

415   plotted near the boundary between alkalic and non-alkalic (Fig. 4a). Two petit-spot basalts (1466R7-

416   001 and R7-003) from the petit-spot knoll were notably silica-undersaturated (i.e., SiO_2 = 39.3–39.4

417   wt%) and classified as foidite (Mikuni et al., 2022). All the western Pacific petit-spot basalts, except

418   for the 1466R7 basalts, were sodic (K_2O/Na_2O = 0.24–0.58) and were notably discriminated to the

419   potassic NW Pacific petit-spots (Fig. 4b).

420   Selected major element oxides and trace element ratios vs. MgO plots for the petit-spot basalts

421   are shown in Figs. 5 and 6, respectively. The MgO concentrations of the 1466R3 and 1521 samples

422   each exhibiting similar petrographic features (i.e., nonvesicular, and glassy) were characterized by

423   values (4.0–4.4 wt%) lower than those of other vesicular samples (6.6–9.3 wt%). The K_2O, Na_2O,

424   Al_2O_3, and SiO_2 contents negatively correlated with MgO (Figs. 5a–d). The CaO, FeO_T, and

425   CaO/Al_2O_3 abundances exhibited positive correlations with MgO (Figs. 5e–g). The TiO_2

426   concentrations exhibited no correlations with MgO (Fig. 5h), as well as the selected trace element

427   ratios (Figs. 6a–g) except for the Sm/Hf ratio with positive correlations (Fig. 6h). The Sm/Hf ratio also

428   negatively correlated with SiO_2 (Fig. S2). The study samples exhibited whole-rock loss on ignition

429   (LOI) in the range of 0.67–1.72 wt%, excluding two relatively altered samples, 1466R7-001 (LOI =

430   2.68 wt%) and R7-003 basalts (LOI = 6.29 wt%).

16

The PM-normalized (Sun and McDonough, 1989) trace element patterns for the petit-spot basalts, including those reported by a previous study (Hirano et al., 2019), were shown for each dive compared to the representative ocean island basalt (OIB) in Figs. 7a–f. The petit-spot basalts generally showed high light rare earth element (LREE)/heavy REE (HREE) ratios. Negative Zr, Hf, Ti, and Y anomalies were commonly observed in these western Pacific petit-spots as well as those of the NW Pacific petit-spots (Fig. 7g). The 1466 basalts collected on the seafloor south of the knoll (1466R3-001 and 1466R3-004 basalts) were compositionally different from those obtained on the knoll (1466R7-001 and 1466R7-003 samples). The basalts from the 6K#1542 and #1544 dives, collected from nearby locations, had the same compositions in major and trace element ratios in both whole rock and glass, respectively (Figs. 4, 5, 6, 7e, and f). These samples in the Ba/Nb and Sm/Hf diagrams were plotted in the range of "Group 3" in the discrimination of the NW Pacific petit-spot basalts (Machida et al., 2015), indicating their negative Zr and Hf anomalies without notable U, Th, Nb, and Ta anomalies in the PM-normalized trace element patterns (Fig. 7h). The Sm/Hf ratio of the differentiated 1466R3 samples was lower than that of other samples. A positive correlation between fluid mobile and immobile elements, Ba vs. Nb (Fig. 8a) and U vs. Th (Fig. 8b), respectively, was observed, excluding the Ba of the 1466R7 samples (Fig. 8a).

Table. 2
Major and trace element compositions of western Pacific petit-spot basalts.

Cruise	YK16-01		YK16-01		YK16-01	YK16-01	YK18-08		YK18-08		YK18-08		YK18-08	YK18-08		YK18-08		YK18-08	
Sample name	6K#1466R3-001		6K#1466R3-004		6K#1466R7-001	6K#1466R7-003	6K#1521R04		6K#1521R05		6K#1522R01		6K#1522R01	6K#1522R02		6K#1522R05		6K#1522R12	
Sample type	Glass		Glass		Whole rock	Whole rock	Glass		Glass		Glass		Whole rock	Glass		Glass		Glass	
Method	EPMA		EPMA		*	*	EPMA		EPMA		EPMA		*	EPMA		EPMA		EPMA	
wt%	mean of n=10	2σ	mean of n=10	2σ			mean of n=10	2σ	mean of n=10	2σ	mean of n=10	2σ		mean of n=10	2σ	mean of n=10	2σ	mean of n=10	2σ
SiO₂	51.56	0.93	50.63	0.79	39.40	39.27	48.42	0.36	46.78	0.97	45.92	1.40	45.28	45.90	0.79	45.38	1.56	46.02	0.69
TiO₂	2.31	0.20	2.19	0.22	3.82	3.68	3.65	0.04	3.32	0.25	2.37	0.17	2.43	2.51	0.20	2.33	0.13	2.45	0.21
Al₂O₃	14.99	0.57	15.10	0.37	11.41	11.46	15.12	0.31	14.38	0.45	12.74	0.23	12.48	12.82	0.25	11.99	0.53	12.91	0.14
Cr₂O₃	-		-		0.03	0.03	-		-		0.01	0.05	0.03	0.02	0.05	0.01	0.05	0.02	0.04
FeOᵀ	9.68	0.30	9.17	0.62	15.12	14.90	10.65	0.29	9.77	0.79	11.72	0.16	12.32	11.64	0.42	10.77	1.02	11.62	0.24
MnO	0.14	0.04	0.14	0.05	0.21	0.20	0.16	0.04	0.14	0.03	0.18	0.04	0.18	0.16	0.04	0.15	0.05	0.17	0.05
MgO	4.04	0.11	3.99	0.11	9.34	7.66	4.43	0.08	4.36	0.10	7.36	0.17	7.26	7.33	0.10	7.12	0.23	7.14	0.16
CaO	7.71	0.11	7.41	0.25	11.19	10.02	8.34	0.68	7.80	0.29	10.72	0.14	11.18	10.81	0.22	10.33	0.68	10.79	0.14
Na₂O	4.61	0.24	4.38	0.50	2.15	2.29	3.84	0.31	4.05	0.55	4.16	0.21	3.53	4.16	0.29	4.16	0.24	4.01	0.46
K₂O	2.31	0.08	2.24	0.12	1.65	2.08	2.25	0.27	2.13	0.12	1.38	0.06	1.42	1.40	0.13	1.31	0.10	1.38	0.04
NiO	0.01	0.03	0.01	0.03	0.03	0.02	-	0.04	-	0.05	0.02	0.03	0.02	0.01	0.04	0.02	0.04	0.02	0.04
P₂O₅	0.93	0.03	0.91	0.06	1.08	1.12	1.53	0.11	1.51	0.03	0.80	0.06	0.83	0.80	0.08	0.82	0.06	0.77	0.04
Total	98.28		96.16		98.10	99.02	98.38		94.24		97.35		98.67	97.56		94.40		97.31	
Mg#	42.64		43.68		52.42	47.82	42.57		44.33		52.83		51.24	52.89		54.11		52.28	
LOI					2.68	6.29							1.72						

FeOᵀ as total values.
Mg# = 100 x Mg / [Mg+Fe²⁺]₍molar₎.
" - ": not detected
*: Analyzed by ActLab

Table. 2 continued

	YK18-08		YK18-08		YK18-08		YK19-05S		YK19-05S	YK19-05S		YK19-05S		YK19-05S		YK19-05S		YK19-05S	YK19-05S		YK19-05S	
	6K#1522R13		6K#1522R16		6K#1522R17		6K#1542R03		6K#1542R03	6K#1542R05		6K#1542R06		6K#1542R09		6K#1544R04		6K#1544R04	6K#1544R05		6K#1544R06	
	Glass		Glass		Glass		Glass		Whole rock	Glass		Glass		Glass		Glass		Whole rock	Glass		Glass	
	EPMA		EPMA		EPMA		EPMA		*	EPMA		EPMA		EPMA		EPMA		*	EPMA		EPMA	
	mean of n=10	2σ	mean of n=10	2σ	mean of n=10	2σ	mean of n=10	2σ		mean of n=10	2σ	mean of n=10	2σ	mean of n=10	2σ	mean of n=10	2σ		mean of n=10	2σ	mean of n=10	2σ
	47.09	0.68	45.22	0.73	45.06	0.98	48.66	1.14	49.35	48.77	1.51	49.66	1.11	50.09	0.93	50.54	0.43	49.08	50.53	0.61	49.59	1.18
	2.50	0.20	2.58	0.20	2.67	0.27	2.11	0.19	2.16	2.13	0.18	2.25	0.22	2.24	0.20	2.04	0.23	2.13	2.08	0.25	2.07	0.24
	13.08	0.33	12.55	0.17	12.55	0.14	13.49	0.18	12.52	13.38	0.19	12.55	0.43	12.78	0.33	13.18	0.12	13.25	12.94	0.34	12.94	0.36
	0.02	0.05	0.01	0.04	0.02	0.08	0.04	0.05	0.05	0.03	0.07	0.02	0.04	0.04	0.04	0.03	0.05	0.05	0.03	0.05	0.03	0.04
	11.74	0.49	11.94	0.40	11.89	0.26	10.60	0.30	11.40	10.47	0.36	10.22	0.51	10.44	0.34	10.46	0.34	11.13	10.77	0.37	10.53	0.49
	0.17	0.05	0.18	0.05	0.18	0.05	0.15	0.04	0.17	0.14	0.04	0.15	0.04	0.16	0.04	0.16	0.02	0.16	0.16	0.05	0.15	0.05
	6.63	0.64	7.24	0.17	7.24	0.17	7.29	0.17	8.18	7.29	0.22	7.03	0.13	7.11	0.12	7.00	0.16	7.50	7.10	0.15	7.05	0.15
	11.01	0.25	11.17	0.24	11.19	0.25	10.03	0.14	10.74	10.00	0.10	9.90	0.32	10.03	0.24	10.63	0.26	10.67	10.36	0.17	10.33	0.22
	4.16	0.36	4.30	0.33	4.28	0.39	3.30	0.28	2.59	3.36	0.24	3.39	0.19	3.26	0.46	3.54	0.25	2.90	3.52	0.26	3.42	0.28
	1.42	0.17	1.52	0.08	1.51	0.06	0.80	0.05	0.77	0.80	0.05	0.89	0.04	0.91	0.06	0.85	0.08	0.85	0.85	0.06	0.83	0.04
	0.01	0.04	0.01	0.04	0.01	0.04	0.01	0.05	0.02	0.02	0.05	0.02	0.05	0.03	0.05	0.02	0.03	0.02	0.01	0.04	0.02	0.04
	0.83	0.05	0.95	0.07	0.95	0.03	0.48	0.04	0.50	0.50	0.04	0.51	0.04	0.52	0.06	0.54	0.03	0.52	0.57	0.05	0.55	0.04
	98.66		97.67		97.54		96.96		99.12	96.91		96.62		97.60		98.98		99.09	98.91		97.50	
	50.18		51.93		52.04		55.07		56.13	55.38		55.07		54.83		54.39		54.57	54.04		54.41	
									0.67									0.83				

Table 3

µg/g	YK16-01 6K#1466R3-001 Glass LA-ICPMS	YK16-01 6K#1466R3-004 Glass LA-ICPMS	YK16-01 6K#1466R7-001 Whole rock *	YK16-01 6K#1466R7-003 Whole rock *	YK18-08 6K#1521R04 Glass LA-ICPMS	YK18-08 6K#1521R05 Glass LA-ICPMS	YK18-08 6K#1522R01 Glass LA-ICPMS	YK18-08 6K#1522R01 Whole rock *	YK18-08 6K#1522R02 Glass LA-ICPMS	YK18-08 6K#1522R05 Glass LA-ICPMS	YK18-08 6K#1522R12 Glass LA-ICPMS
Li	7.60	7.32			7.39	7.00	8.10		7.69	7.83	7.71
B	2.92	3.17			3.05	3.48	2.38		2.34	2.78	2.69
Sc	14.9	15.2	25.0	25.0	15.7	15.4	20.1	21.0	20.6	21.2	21.1
V	159	160	353	324	167	157	204	234	208	207	207
Cr	36.8	37.1	200	190	0.52	0.48	215	190	218	213	222
Co	29.7	29.9	61.0	57.0	32.8	31.2	46.2	49.0	46.8	46.1	47.3
Rb	47.5	47.6	26.0	32.0	34.1	33.4	25.8	28.0	26.9	26.8	26.6
Sr	976	991	577	307	1385	1361	848	827	924	943	901
Y	21.8	22.2	37.0	58.0	33.1	32.2	24.4	25.0	26.0	27.6	26.7
Zr	254	260	259	248	293	286	157	163	168	177	171
Nb	56.4	57.5	65.0	64.0	58.7	57.6	49.5	52.0	55.3	55.7	54.6
Cs	0.58	0.58	-	-	0.35	0.34	0.32	-	0.35	0.37	0.34
Ba	613	623	453	317	577	565	447	479	512	528	500
La	44.1	45.4	65.2	90.8	44.2	42.8	42.8	51.5	49.6	51.4	48.6
Ce	93.2	95.0	138	164	105	101	88.1	110	101	103	98.3
Pr	10.6	10.8	16.6	23.8	13.4	13.0	9.9	12.4	11.3	11.6	11.2
Nd	42.5	43.7	62.6	89.3	59.5	57.6	39.4	47.4	45.5	47.5	45.7
Sm	8.39	8.65	12.0	17.6	12.8	12.3	8.27	10.1	9.60	9.83	9.60
Eu	2.78	2.83	3.76	5.38	4.17	4.03	2.72	3.39	3.13	3.19	3.14
Gd	7.08	7.23	10.7	15.7	11.0	10.6	7.12	9.20	8.27	8.93	8.53
Tb	0.89	0.94	1.50	2.30	1.40	1.35	0.93	1.30	1.08	1.14	1.10
Dy	4.84	4.99	8.00	12.2	7.55	7.31	5.05	6.60	5.94	6.23	6.05
Ho	0.79	0.81	1.30	2.10	1.24	1.19	0.82	1.10	0.97	1.01	1.00
Er	1.96	2.04	3.30	5.30	3.01	2.94	2.03	2.60	2.37	2.53	2.41
Tm	0.23	0.25	0.44	0.69	0.34	0.34	0.22	0.31	0.26	0.29	0.27
Yb	1.43	1.48	2.60	4.10	2.12	2.02	1.40	1.70	1.64	1.71	1.69
Lu	0.19	0.19	0.36	0.60	0.28	0.26	0.18	0.24	0.22	0.23	0.22
Hf	5.33	5.54	5.80	6.20	6.42	6.12	3.14	3.90	3.76	4.01	3.92
Ta	3.04	2.81	4.80	5.30	3.34	2.93	2.01	2.80	2.34	2.35	2.37
Pb	3.55	3.39	-	6.00	2.82	2.59	3.06	-	3.68	3.64	3.59
Th	4.87	5.11	7.70	7.70	3.52	3.40	4.65	6.40	5.73	6.07	5.69
U	1.29	1.29	1.40	7.70	0.97	0.91	1.08	6.40	1.28	1.27	1.26

* - *: not detected
*: Analyzed by ActLab

Table. 3 continued

|	YK18-08 6K#1522R13 Glass LA-ICPMS	YK18-08 6K#1522R16 Glass LA-ICPMS	YK18-08 6K#1522R17 Glass LA-ICPMS	YK19-05S 6K#1542R03 Glass LA-ICPMS	YK19-05S 6K#1542R03 Whole rock *	YK19-05S 6K#1542R05 Glass LA-ICPMS	YK19-05S 6K#1542R06 Glass LA-ICPMS	YK19-05S 6K#1542R09 Glass LA-ICPMS	YK19-05S 6K#1544R04 Glass LA-ICPMS	YK19-05S 6K#1544R04 Whole rock *	YK19-05S 6K#1544R05 Glass LA-ICPMS	YK19-05S 6K#1544R06 Glass LA-ICPMS
Li	8.06	8.53	8.42	5.54		5.52	6.00	6.19	6.21		6.20	6.16
B	2.83	2.77	2.94	1.60		1.88	1.89	1.80	2.28		2.38	2.14
Sc	21.5	19.7	20.6	22.5	24.0	22.3	22.7	23.7	22.0	22.0	22.8	23.6
V	217	213	209	189	222	188	200	201	203	215	197	191
Cr	231	203	203	334	350	317	269	267	292	330	285	273
Co	44.3	47.2	46.8	42.3	49.0	42.7	42.1	41.8	44.9	47.0	43.4	42.0
Rb	28.0	30.3	29.7	14.2	14.0	14.5	17.4	17.4	17.0	17.0	16.4	
Sr	930	1063	1086	565	487	568	622	643	579	519	595	604
Y	27.0	27.9	29.6	22.8	20.0	22.4	22.5	23.7	22.9	21.0	24.0	25.1
Zr	173	184	194	122	120	122	134	140	123	122	128	132
Nb	55.7	64.2	65.7	24.0	23.0	24.0	25.1	25.9	27.0	25.0	27.3	27.4
Cs	0.36	0.41	0.40	0.18		0.20	0.22	0.21	0.25		0.25	0.23
Ba	514	584	590	255	219	254	292	301	286	259	297	297
La	49.3	58.1	60.9	26.8	26.1	26.6	28.6	29.8	27.8	28.0	28.8	29.5
Ce	101	120	122	56.6	62.8	56.5	58.8	60.4	59.8	66	60.9	60.0
Pr	11.5	13.3	13.8	6.86	7.37	6.79	7.10	7.42	7.20	7.60	7.34	7.41
Nd	46.6	53.3	55.7	29.3	30.0	29.0	30.3	31.7	30.4	31.3	31.3	31.8
Sm	9.71	10.8	11.4	6.65	7.00	6.64	6.82	7.21	6.79	7.10	7.10	7.27
Eu	3.21	3.58	3.67	2.24	2.41	2.23	2.28	2.38	2.34	2.42	2.39	2.44
Gd	8.57	9.42	9.92	6.29	6.80	6.26	6.53	6.82	6.45	6.90	6.75	6.90
Tb	1.12	1.20	1.27	0.85	1.00	0.85	0.87	0.93	0.89	1.00	0.91	0.96
Dy	6.10	6.38	6.81	4.89	5.30	4.83	4.88	5.10	4.91	5.40	5.17	5.33
Ho	1.00	1.02	1.10	0.83	0.90	0.82	0.84	0.87	0.84	0.90	0.89	0.91
Er	2.46	2.47	2.63	2.12	2.30	2.13	2.10	2.22	2.10	2.30	2.27	2.32
Tm	0.28	0.28	0.30	0.26	0.28	0.26	0.26	0.26	0.26	0.29	0.28	0.27
Yb	1.70	1.67	1.75	1.57	1.70	1.57	1.52	1.60	1.58	1.70	1.66	1.71
Lu	0.22	0.21	0.22	0.21	0.23	0.21	0.20	0.22	0.21	0.22	0.23	0.23
Hf	3.95	4.08	4.36	2.95	3.10	2.95	3.20	3.39	2.95	3.00	3.12	3.18
Ta	2.40	2.63	2.77	1.08	1.30	1.10	1.16	1.23	1.21	1.40	1.23	1.24
Pb	3.71	4.38	4.29	1.67		1.76	1.82	1.85	1.94		1.98	1.82
Th	5.69	6.88	7.29	2.47	2.80	2.47	2.78	2.89	2.72	3.00	2.85	2.95
U	1.31	1.57	1.58	0.62	2.80	0.63	0.66	0.66	0.71	3.00	0.68	0.65
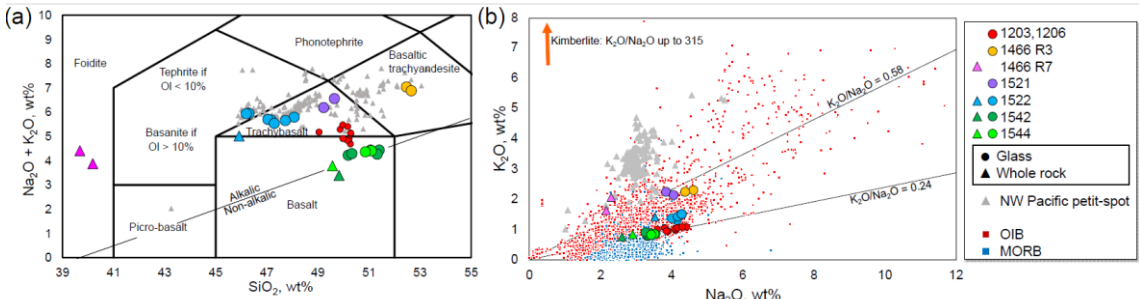
Fig. 4. Relationships between the SiO₂ and alkali contents. (a) Total alkali vs. silica diagram using the platform of Le Bas et al. (1986). The dividing line of alkaline and sub-alkaline is from Irvine and Baragar (1971). The data are plotted as the total 100 wt%. The triangles and circles show the whole-rock and quenched-glass compositions, respectively. The compositions of the NW Pacific petit-spots are represented by gray triangles (Hirano and Machida, 2022). The data of the 1203 and 1206 basalts are from Hirano et al. (2019), and those of the 1466R7 basalts are from Mikuni et al. (2022). (b) K_2O vs. Na_2O diagram. The maximum K_2O/Na_2O value of kimberlite is from PetDB database (https://search.earthchem.org/). The data of OIB and MORB are compiled from Stracke et al. (2022) as "Expert datasets" in GEOROC database (https://georoc.eu/georoc/new-start.asp).
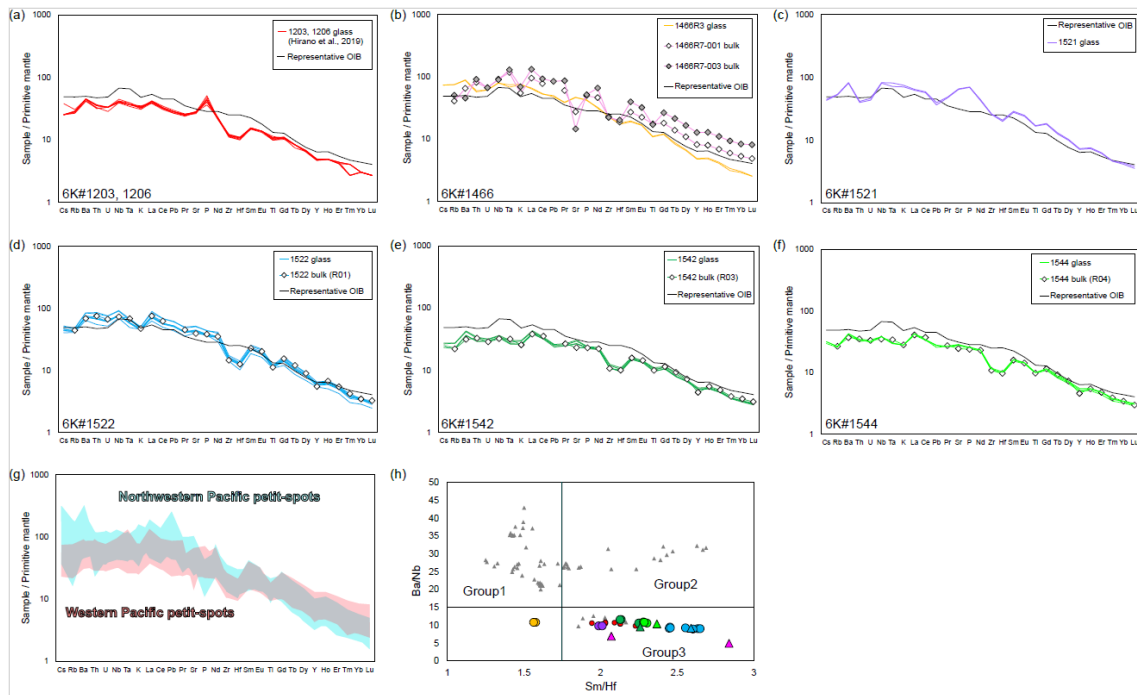
462

463
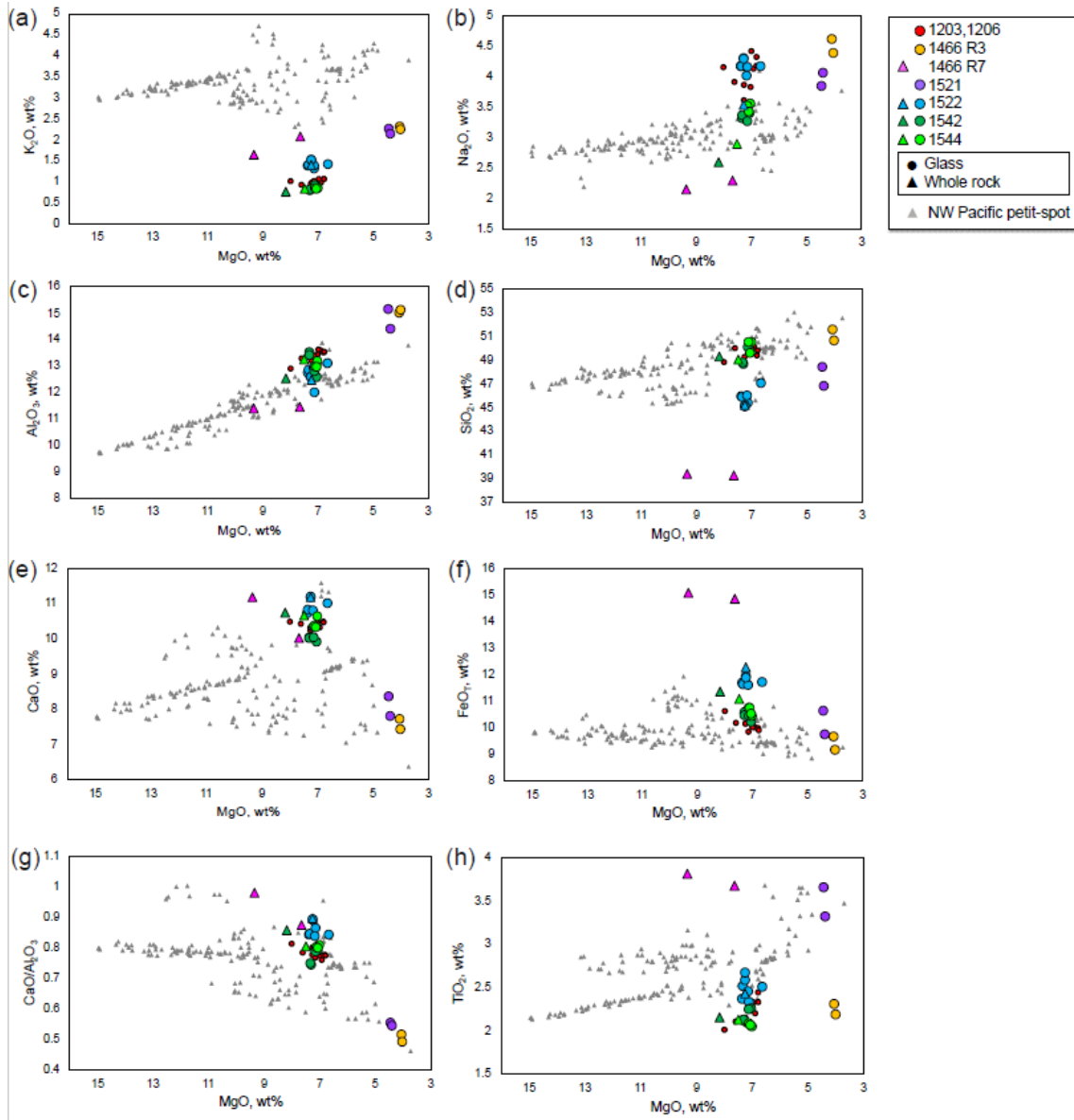
Fig. 5. Selected major-element oxides against MgO. The symbols and compiled data correspond to those in Fig. 3.

19
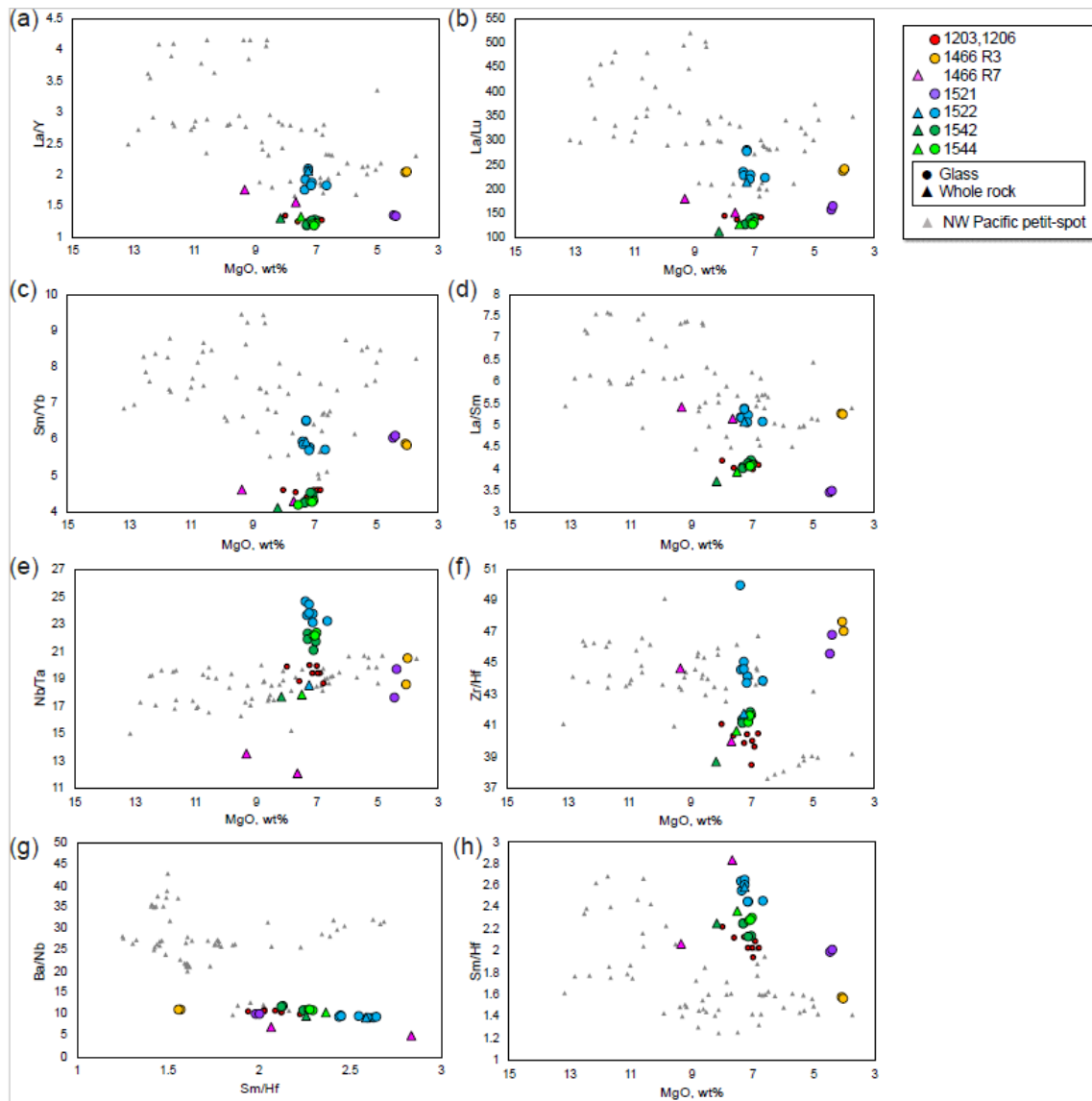
Fig. 6. Selected trace-element ratios against MgO. The symbols and compiled data correspond to those in Fig. 3.

Fig. 7. Primitive mantle (PM, Sun and McDonough, 1989)-normalized trace-element patterns (a)–(g) and element ratios (h). (g) The compositional range of the study samples and NW Pacific petit-spots (Hirano and Machida, 2022). (h) The Ba/Nb and Sm/Hf ratios of the petit-spot basalts to discriminate the three groups after Machida et al. (2015). The data of 1203, 1206 basalts and 1466R7 basalts are from Hirano et al. (2019) and Mikuni et al. (2022), respectively. The symbols and compiled data in the (h) correspond to those in Fig. 3.
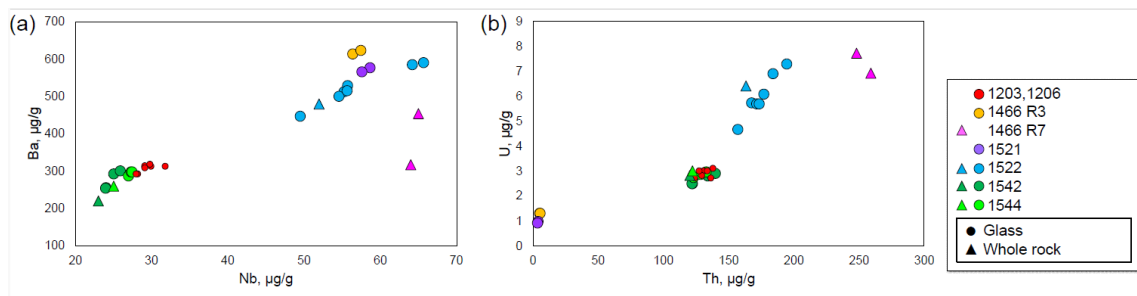

Fig. 8. Alteration sensitive elements (Ba and U) vs. insensitive elements (Nb and Th). The symbols and compiled data correspond to those in Fig. 3.

## 5.2 Sr–Nd–Pb isotopic composition

The Sr, Nd, and Pb isotopic compositions of the leached, unleached whole rock, and fresh glasses

21

484 in this study (presented in Table 4) were in practically identical ranges of $^{87}Sr/^{86}Sr$ (0.703412–

485 0.704424), $^{143}Nd/^{144}Nd$ (0.512694–0.512890), $^{206}Pb/^{204}Pb$ (18.6582–18.7778), $^{207}Pb/^{204}Pb$ (15.5086–

486 15.5749), and $^{208}Pb/^{204}Pb$ (38.6506–38.8041) despite their different locations (Figs. 9a–d, Table 4).

487 The isotopic compositions of the quenched glass and whole rock were identical, indicating that the

488 characteristics of the melting source could be obtained through the geochemistry of the young and

489 fresh volcanic quenched glass. The leached and unleached materials of the same sample also had

490 similar isotopic ratios, except for the 1466R7-003 basalt, which had a relatively high LOI (6.29 wt%)

491 (Figs. 9a–d). The Sr–Nd–Pb isotopic three-dimensional (3D) plot is shown in Fig. 9e.

492
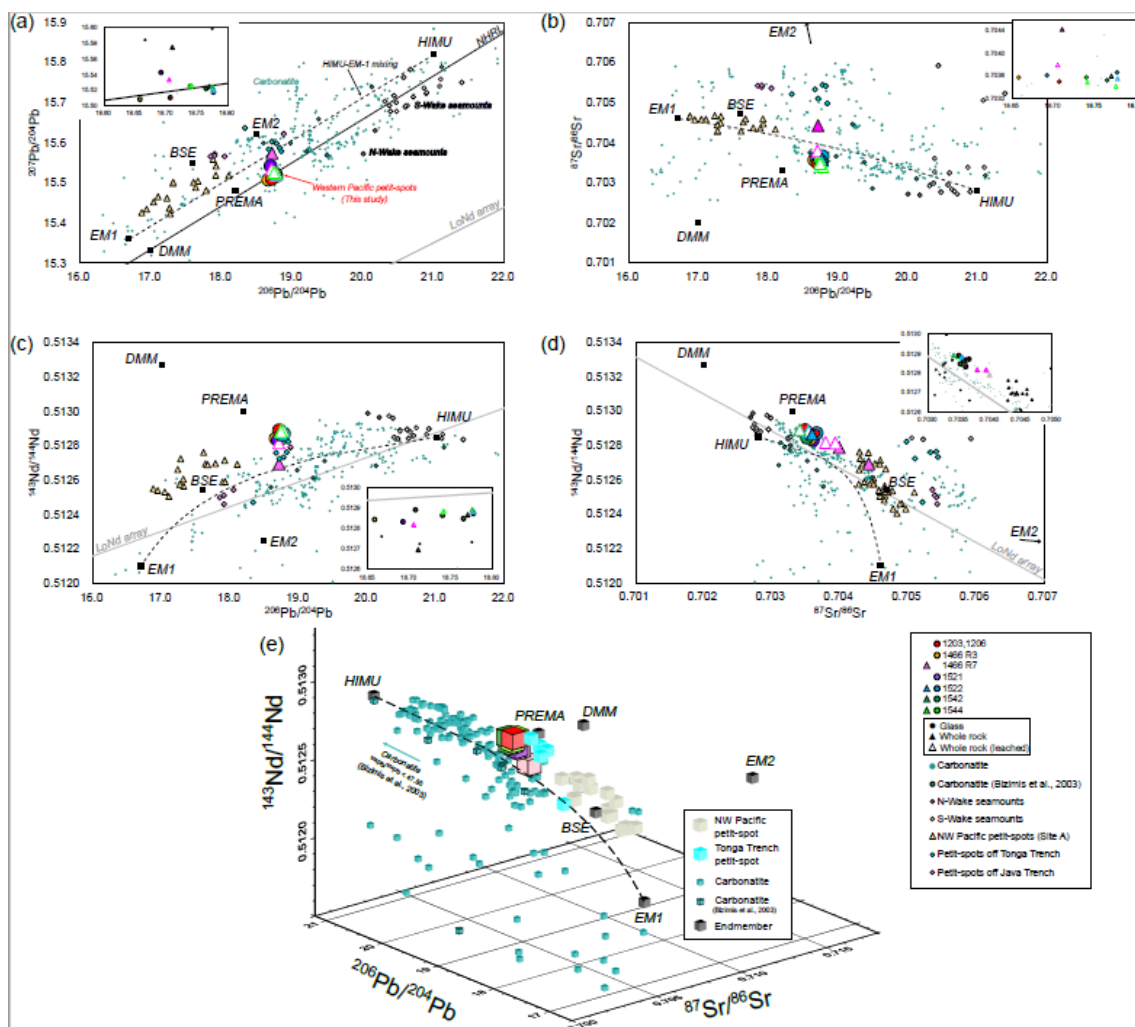
494 Fig. 9. Sr–Nd–Pb isotopic variations of the petit-spot basalts. The mantle endmembers are derived from a study by

495 Zindler and Hart (1986). The open triangles in (a)–(d) represent the acid-leached samples. Carbonatite

496 data were compiled from GEOROC (https://georoc.eu/georoc/new-start.asp) with Bizimis et al. (2003).

497 Carbonatite data with $^{87}Sr/^{86}Sr$ > 0.706 by GEOROC were eliminated. The northwestern (NW) Pacific

498 petit-spots and petit-spots off the Tonga Trench are from Hirano and Machida (2022) and Reinhard et al.

499   (2019), respectively. The petit-spots off the Java trench are from Taneja et al. (2016) and Falloon et al.

500   (2022). The data of 1203 and 1206 basalts are from Hirano et al. (2019). The data of the Wake seamounts

501   are from studies by Konovalov and Martynov (1992), Koppers et al. (2003), Konter et al. (2008), Natland

502   (1976), Smith et al. (1989), and Staudigel et al. (1991). The northern hemisphere reference line (NHRL)

503   and Low Nd (LoNd) arrays are from studies by Hart (1984) and Hart et al. (1986), respectively. (e) The

504   three-dimensional (3D) plot of the Sr–Nd–Pb isotopic compositions. The compilation and mantle

505   endmembers correspond to (a)–(d). The color usages of the plots were the same as (a)–(d).

506

Table. 4
Sr, Nd, and Pb isotopic compositions of western Pacific petit-spot basalts and measured standards.

Cruise	Sample name	Sample type	$^{87}Sr/^{86}Sr$	$^{143}Nd/^{144}Nd$	$^{206}Pb/^{204}Pb$	$^{207}Pb/^{204}Pb$	$^{208}Pb/^{204}Pb$
YK16-01	6K#1466 R3-004	Glass	0.703568 (06)	0.512842 (05)	18.6582 (07)	15.5086 (06)	38.6506 (19)
YK16-01	6K#1466 R7-001	Whole rock leached	0.703790 (05)	0.512817 (07)	18.7054 (20)	15.5337 (20)	38.8041 (50)
YK16-01	6K#1466 R7-001	Whole rock unleached	0.703989 (05)	0.512790 (06)			
YK16-01	6K#1466 R7-003	Whole rock leached	0.703933 (11)	0.512815 (05)			
YK16-01	6K#1466 R7-003	Whole rock unleached	0.704424 (05)	0.512694 (05)	18.7107 (06)	15.5749 (06)	38.7618 (17)
YK18-08	6K#1521 R04	Glass	0.703605 (05)	0.512832 (04)	18.6924 (06)	15.5428 (06)	38.7005 (19)
YK18-08	6K#1522 R01	Whole rock leached	0.703544 (05)	0.512881 (06)	18.7778 (09)	15.5209 (08)	38.7991 (22)
YK18-08	6K#1522 R01	Whole rock unleached	0.703590 (05)	0.512866 (06)	18.7705 (07)	15.5248 (07)	38.7905 (22)
YK18-08	6K#1522 R01	Glass	0.703656 (06)	0.512872 (04)	18.7773 (08)	15.5178 (07)	38.7904 (21)
YK19-05S	6K#1542 R03	Whole rock leached	0.703412 (07)	0.512890 (06)	18.7759 (10)	15.5244 (11)	38.7574 (36)
YK19-05S	6K#1542 R05	Glass	0.703517 (06)	0.512847 (04)	18.7653 (08)	15.5224 (07)	38.7345 (19)
YK19-05S	6K#1544 R04	Whole rock leached	0.703480 (04)	0.512883 (05)	18.7413 (14)	15.5262 (14)	38.745 (41)
YK19-05S	6K#1544 R04	Glass	0.703568 (05)	0.512863 (04)	18.7400 (08)	15.5253 (09)	38.7347 (22)
YK10-05	6K#1206 R04	Glass	0.703492 (05)	0.512890 (04)	18.7074 (06)	15.5109 (07)	38.6970 (19)
YK10-05	6K#1206 R04 duplicate	Glass			18.7071 (07)	15.5119 (07)	38.6950 (18)

Type of value	Standered for each isotope		$^{87}Sr/^{86}Sr$	$^{143}Nd/^{144}Nd$	$^{206}Pb/^{204}Pb$	$^{207}Pb/^{204}Pb$	$^{208}Pb/^{204}Pb$
Analyzed value	JB-2		0.703721 (05)	0.513094 (04)	18.3326 (05)	15.5453 (06)	38.2240 (17)
Reference value	JB-2	Sr, Nd: Orihashi et al. (1998), Pb: Tanimizu and Ishikawa (2006)	0.703709 (29)	0.513085 (08)	18.3315 (25)	15.5460 (21)	38.2240 (55)
Analyzed value	JNdi-1	(n=2)		0.512103 (05)			
Reference value	JNdi-1	Wakaki et al. (2007)		0.512101 (11)			
Analyzed value	SRM987	(n=2)	0.710239 (05)				
Reference value	SRM987	Weis et al. (2006)	0.710254 (02)				
Analyzed value	SRM981				16.9303 (05)	15.4828 (06)	36.6710 (16)
Reference value	SRM981	Tanimizu and Ishikawa (2006)			16.9308 (10)	15.4839 (11)	36.6743 (30)

507 Errors shown in parentheses represent 2σ and apply to the last two digits.

508

5.3 Age determination and estimation

510

511   The $^{40}Ar/^{39}Ar$ ages were determined for two samples (1466R6-001 and 1522R01) (Fig. 10a,

512 Table S4). The secondary material (e.g., alteration products) plausibly causes the recoil loss and

513 redistribution of Ar during irradiation of samples, particularly fine-grained groundmass separates of

514 submarine basalt (Koppers et al., 2000). This effect is negligible for $^{40}Ar/^{39}Ar$ dating samples in this

515 study because the total K/Ca ratios estimated using the irradiated $^{39}Ar_K/^{37}Ar_{Ca}$ ratio (0.089 for 1466R6,

516 0.080 for 1522R01; Table S4) are mostly correspond to the bulk K/Ca ratios calculated using the major

517 element compositions of Table 2 (0.088 for 1466R6-001, 0.076 for 1522R01). This is supported by

518 the rock descriptions recognized no secondary materials of crystalline $^{40}Ar/^{39}Ar$ specimens. The

519   1466R6-001 sample had a plateau age of 3.03 ± 0.18 Ma in seven fractions comprising 94.1% released

520   ^{39}Ar. However, the plateau age was recognized as apparently old, owing to excess ^{40}Ar, as indicated

521   by the initial ^{40}Ar/^{36}Ar ratio of 325 ± 15, which exceeded the atmospheric ratio (296.0; Nier, 1950) in

522   the inverse isochron. The inverse isochron age of 2.56 ± 0.34 Ma showed the best age estimate for the

523   1466R6-001 basalt (Fig. 10a). The 1522R01 sample released almost no radiogenic daughter nuclide

524   of ^{40}Ar in the K–Ar age system (Fig. 10a).

525   The ranges of eruption age were estimated for all the samples using the average thickness (n =

526   20) of ferromanganese crust and palagonite rind (hydrated quenched glass) with their

527   deposition/formation rates on the seafloor (ferromanganese crust, 1–10 mm/Myr; Hein et al., 1999;

528   palagonite, 0.03–0.3 mm/Myr; Moore et al., 1985) (Fig. 10b). Using this approach, the western Pacific

529   petit-spots were expected to have erupted later than ca. 9 Ma. The ranges of eruption age estimated

530   from palagonite rind did not overlap with those from ferromanganese crust showing older durations,

531   although they had general correlations (Fig. 10b). The ^{40}Ar/^{39}Ar ages of two samples and the U-Pb

532   age of zircon in the 1203 and 1206 peperites (Hirano et al., 2019) were overlaid within these ranges.

533
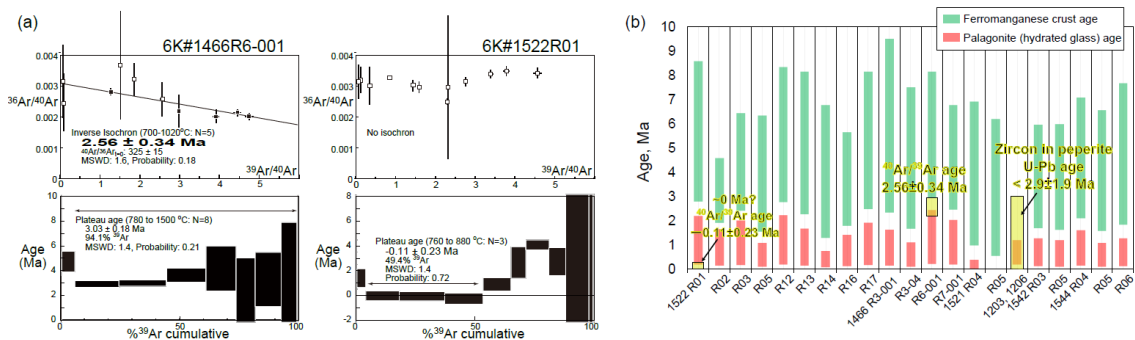
535 Fig. 10. Geochronological data. (a) The ^{40}Ar/^{39}Ar ages of the 6K#1466R6-001 and 6K#1522R01 basalts. The errors

536   show a 2-sigma confidence level. (b) Estimated relative ages using the thickness of ferromanganese crust

537   (green bands) and palagonite (hydrated quenched-glass rind; red bands) covered with petit-spot basalts.

538   These values were estimated using the average for each sample (n = 20). The U-Pb age of zircon in the

539   6K#1203 and 1206 peperites are from Hirano et al. (2019).

540

541 **6 Discussion**

542

543 **6.1 Eruptive setting of western Pacific petit-spots**

544

545   In this study, two crystalline petit-spot basalts were subjected to ^{40}Ar/^{39}Ar dating. A previously

546 investigated petit-spot knoll in this region (examined during the 6K#1203 and #1206 dives) was dated

547 at "younger than 3 Ma" through the U–Pb dating of eight zircons in peperites (Fig. 10b) (Hirano et al.,

24

548   2019). The results revealed that the silica-undersaturated vesicular basalt of 1466R6-001, hosting

549   ultramafic xenoliths (Mikuni et al., 2022), exhibited a $^{40}Ar/^{39}Ar$ age of 2.56 ± 0.34 Ma (Fig. 10). On

550   the contrary, the fresh vesicular basalt of 1522R01, which erupted at the foot of the 100-Ma Takuyo-

551   Daigo seamount (Fig. 2) (Nozaki et al., 2016), did not exhibit radiogenic ^{40}Ar indicating its young age

552   (~0 Ma) (Fig. 10). The ranges of eruption ages were estimated using the average thickness of

553   ferromanganese crust and palagonite rind (seawater-hydrated quenched glass) with their

554   deposition/formation rates on the seafloor. The $^{40}Ar/^{39}Ar$ and zircon U–Pb ages were within these

555   ranges (Fig. 10). The petit-spot volcanic field is surrounded by Cretaceous seamounts (Koppers et al.,

556   2003) and irregular Paleogene volcanoes (Aftabuzzaman et al., 2021; Hirano et al., 2021). However,

557   no zero-aged hotspots were observed in this region, and the P-wave tomographic image of the surface

558   to the core–mantle boundary of the study area did not exhibit a plume-like low-velocity zone (Fig. 1c;

559   Lu et al., 2019). Furthermore, the MORB-like to more depleted noble-gas isotopic compositions of

560   the petit-spot knoll (investigated by 6K#1203 and #1206 dives) suggested its upper mantle origin

561   (Yamamoto et al., 2018). Along with the outer-rise bulge in front of the Mariana Trench detected

562   through a positive gravitational anomaly (Hirano et al., 2019), these data suggest that the western

563   Pacific petit-spot volcanoes could have erupted at ~0–3 Ma owing to the flexure of the subducting

564   Pacific Plate into the Mariana and Ogasawara Trenches.

565   The petit-spot basalts from the 6K#1542 and #1544 dives could have originated from the same

566   eruptive source based on their similar petrographic and geochemical features despite a distance of ~6.8

567   km between both (Figs. 3d, 4, 5, 6, 7, 8, and 9). Contrarily, in terms of their petrography and

568   geochemistry, the basalts from the 6K#1466 dive are distinguished between the samples from the lava

569   flows on the abyssal plain (1466R3-001 and 1466R3-004 samples) and the samples from the knoll site

570   (1466R6-001, 1466R7-001, and 1466R7-003 samples). The 1466R3 basalts were collected at a lava

571   outcrop 600 m south of the knoll, and the 1466R6 and 1466R7 samples were collected on the western

572   slope of the knoll (Fig. 3a). The 1466R3 series are glassy with a high SiO_2 content (50.6–51.6 wt%),

573   including minor plagioclase and fewer vesicles (Figs. 3a and 4a). However, the 1466R6–R7 series

574   exhibited silica-undersaturated compositions (SiO_2 = 39.3–39.4 wt%) and high vesicularities (20–40

575   vol.%) (Figs. 3b and 4a). Combining these observations with the differences in MgO contents and

576   trace element compositions, the 1466R3 and 1466R6–R7 basalts are implied to have different parental

577   magmas (Figs. 6 and 7b). Generally, vesicular samples (1203, 1206, 1466R7, 1522, 1542, and 1544

578   basalts) are relatively primary (i.e., MgO > 6.63 wt%), whereas nonvesicular samples (1466R3 and

579   1521 basalts) are evolved (i.e., MgO < 4.43 wt%). This correlates with the compositions of olivine

580   microphenocrysts in the low forsterite content (Fo# = $100 \times Mg/[Mg+Fe^{2+}]_{cation}$) of olivine in evolved

581   basalts and the high Fo# of olivine in the relatively primary basalts (Figs. S1a–c).

582   The CI chondrite-normalized REE ratios of these samples are within those of OIBs, and the

583   REE patterns exhibit HREE-depleted patterns (Fig. S3). However, among the western Pacific petit-

584   spots, each volcano shows distinct REE and trace element ratios (i.e., parental magmas) (Figs. 6 and
585   S3). Considering the absence of correlation between MgO and the trace element ratios, it is suggested
586   that each volcano could have originated from isolated sources (i.e., melt ponds) with varying chemical
587   compositions and degrees of melting (Fig.6). On the contrary, the radiogenic Sr, Nd, and Pb isotopic
588   ratios of the samples are nearly identical, indicating equivalent components in the source (Fig. 9).
589   In summarily, (1) the western Pacific petit-spot volcanoes erupted at ~0–3 Ma owing to the plate
590   flexure related to the subduction of the Pacific Plate into the Mariana Trench (Figs. 1 and 2). (2) The
591   1542 and 1544 samples originated during the same magmatic event (Fig. 3d). However, the basalts
592   from the 6K#1466 dive were divided into two parental magmas (1466R3 and 1466R6–R7 basalts)
593   (Fig. 3a). (3) Each volcano originated from an isolated source and/or ascending processes, as indicated
594   by independent trace element ratios. Despite this, the geochemical components involved in the source
595   were similar among the western Pacific petit-spot volcanoes due to the nearly identical Sr, Nd, and Pb
596   isotopic compositions (Figs. 6 and 9). The variation in trace element compositions among the
597   volcanoes is plausibly attributed to the degree of contribution of carbonatite flux and/or the recycled
598   crustal component to the source, as discussed below.
599

600   **6.2 Petit-spot magma composition and its evaluation**
601

602   Post-eruption alteration in seawater may have affected the chemical composition of oceanic
603   basalts. Thus, various approaches, including petrographic observation, geochemical investigation, and
604   acid leaching, have been employed to evaluate the primary features and the removal of this effect for
605   isotopic analysis (Hanano et al., 2009; Melson et al., 1968; Miyashiro et al., 1971; Nobre Silva et al.,
606   2009; Resing and Sansone, 1999; Staudigel and Hart, 1983; Zakharov et al., 2021). The study samples
607   exhibit whole-rock LOI of <1.72 wt%, except for two relatively altered samples, 1466R7-001 (LOI =
608   2.68 wt%) and R7-003 (LOI = 6.29 wt%) basalts. Pristine quenched glasses are preserved in most of
609   the samples, excluding three exceptional samples (1466R6-001, R7-001, and R7-003 basalts). Positive
610   correlations exist between the alteration-insensitive (e.g., Nb and Th) and -sensitive (e.g., Ba and U)
611   incompatible elements, indicating that the effect of seawater alteration was not extensive, except for
612   the 1466R7-001 and R7-003 basalts (Fig. 8). Despite originating from different volcanic edifices, the
613   positive correlation of all the study samples is attributed to the chemical similarity of source
614   compositions for certain elements (i.e., the Ba/Nb and U/Th ratios are nearly constant among the
615   samples) as well as the Sr, Nd, and Pb isotopic compositions (Fig. 9). These findings demonstrate that
616   most of the petit-spot basalts were largely unaffected by seawater alteration, with a few exceptions,
617   i.e., 1466R7-001 and R7-003 basalts.
618   The MgO (4–9 wt%), Ni (<263 ppm), and Cr (<350 ppm) contents in the samples are lower than
619   the expected values of primary mantle-derived melt (MgO >10 wt%, Ni >400 ppm, Cr >1000 ppm;

26

Frey et al., 1978). Similarly, the Mg# ($100 \times$ Mg/[Fe^{2+} + Mg]$_{molar}$) values range from 41 to 57 (Table 2) against the primary basaltic melt, which is equilibrated with the upper mantle (Mg# = 66–75; Irving and Green, 1976). No phenocrysts were observed (only microphenocryst), despite such differentiated compositions as well as most of the NW Pacific petit-spot basalts. This suggests that the western Pacific petit-spots experienced crystal fractionation in the lithosphere as well as the case in the NW Pacific petit-spot (Machida et al., 2017; Valentine and Hirano, 2010; Hirano, 2011; Yamamoto et al., 2014). Consequently, calculating the primary composition of the petit-spot basalts using the mineral modal composition on the thin section was not possible. However, the major element trends of the samples indicate the crystal fractionation of the same phases. Negative trends of the Al$_2$O$_3$ content and the positive trends in CaO and CaO/Al$_2$O$_3$ content with decreasing MgO indicate the occurrence of olivine, spinel, and clinopyroxene fractionation (Figs. 5c, e, and g). The absence of visible correlations of K$_2$O, Na$_2$O, SiO$_2$, and TiO$_2$ contents against MgO suggests insignificant fractionation of plagioclase and Fe–Ti oxides. The Fe–Ti oxides as minor phases in the groundmasses and plagioclases were only observed in the most differentiated 1466R3-001 and R3-004 basalts (Figs. 3, 5a, b, d, and h). However, these major elemental trends should be interpreted as apparent because each petit-spot volcano originated from an isolated parental magma with a different chemical composition or degree of partial melting, as discussed above.

The melting source of alkali basalts can be determined more effectively by examining their trace element composition rather than major elements (Hofmann, 2003; Machida et al., 2014, 2015). Trace element composition of magma, however, could be modified by crustal and/or mantle assimilation and fractionation of specific minerals. The relatively primitive basalts (1203, 1206, 1466R6, R7, 1522, 1542, and 1544 samples) contained xenocrystic olivines and partly ultramafic xenoliths, suggesting a rapid magma ascent (Hirano et al., 2019; Mikuni et al., 2022; Fig. S4). However, since the stagnation of ascending petit-spot magma could lead to the formation of fertile peridotite and pyroxene-rich veins in the middle to lower depths of the lithosphere (Mikuni et al., 2022; Pilet et al., 2016), the chemical composition of the petit-spot magma could be modified through assimilation with ambient lithospheric peridotite. According to Hirano and Machida (2022), ascending silica-undersaturated melt would predominantly consume orthopyroxene (±spinel) and result in a more silicic composition with Zr and Hf depletion. This is due to the relatively higher Zr–Hf partition of orthopyroxene than compared to other trace elements (Pilet et al., 2008; Shaw, 1999; Tamura et al., 2019). The orthopyroxenes of fertile pyroxenites and lherzolite xenoliths metasomatized by petit-spot melts exhibit Zr and Hf enrichment (Mikuni et al., 2022; Fig. S5). If this silica-enrichment (i.e., melt–rock interaction) was significant, a positive correlation between SiO$_2$ and Sm/Hf is expected as a mantle assimilation trend. However, the samples exhibited a negative correlation, similar to those of the NW Pacific petit-spots (Hirano and Machida, 2022) (Fig. S2). Considering the relation between the Sm and Hf partition coefficients of clinopyroxene (i.e., $D^{Hf} < D^{Sm}$; McKenzie and O'Nions, 1991; Kelemen et al., 2003), we suggest that

656　the negative correlation between the Sm/Hf and SiO_2 in the petit-spot basalts probably reflects the

657　crystal fractionation of clinopyroxene rather than mantle assimilation. The Ba/Nb ratios of the samples

658　are nearly constant and do not correlate with the MgO and SiO_2 contents (Figs. 6g and S2g). The lack

659　of correlation between other trace element ratios, excluding Sm/Hf and Ba/Nb (i.e., La/Y, La/Lu,

660　Sm/Yb, La/Sm, Nb/Ta, Zr/Hf), and the MgO concentration suggests that crystal fractionation may not

661　have been involved in those of the incipient melt (Fig. 6). However, independently tracking the

662　evolution of the trace element composition for each volcano is challenging, given that each volcano

663　originated from isolated sources. Thus, considering the observations above, the fresh and zero-aged

664　1522 basalts (having the highest Sm/Hf ratios and lowest SiO_2 contents among the fresh samples and

665　higher MgO contents) were selected for further analysis with geochemical modeling. Given that the

666　1522 samples had MgO in the range of 6.63–7.36 wt%, olivine was expected to be the dominant phase

667　of crystal fractionation (Asimow and Langmuir, 2003; Helz and Thornber, 1987; Herzberg, 2006). By

668　applying the olivine maximum fractionation model (Takahashi et al., 1986; Tatsumi et al., 1983) to

669　test two samples, it was noted that 7–9% olivine addition was required to achieve the olivine

670　composition corresponding to "Mantle olivine array" in the NiO and Fo# spaces (Figs. S6a, b). The

671　calculated primary trace element contents did not considerably differ from those of the analytical

672　compositions (Table S5 and Fig. S6). Thus, the 1522 basalts were assumed to be the most primary

673　petit-spot basalt samples and were used to evaluate the geochemical modeling results.

674

6.3 Melting source of western Pacific petit-spots

676

677　　　The depletions observed in specific elements (e.g., Ta, Zr, Hf, and Ti) in the petit-spot basalts

678　potentially demonstrate the involvement of carbonatitic materials in conjunction with a large amount

679　of CO_2 and lower Mg isotopic ratio than that of the normal mantle (Bizimis et al., 2003; Dasgupta et

680　al., 2009; Hirano and Machida, 2022; Hoernle et al., 2002; Liu et al., 2020; Okumura and Hirano,

681　2013). Other oceanic lavas originating from the asthenosphere (e.g., Hawaiian rejuvenated lavas and

682　North Arch volcanoes) exhibited characteristic trace element signatures (i.e., Zr and Hf depletion)

683　similar to those of petit-spot lavas. This implies that their melting sources were involved with

684　carbonatitic materials with or without plume-derived components (Fig. S7; Borisova and Tilhac, 2021;

685　Clague and Frey, 1982; Clague et al., 1990; Dixon et al., 2008; Yang et al., 2003). Additionally, the

686　involvement of recycled crustal components was inferred from the geochemical features of the petit-

687　spot basalts, and the upper mantle was revealed to be heterogeneous (Liu et al., 2020; Machida et al.,

688　2009, 2015). Such a scenario of the source for petit-spot magma aligns with the previously suggested

689　petrogenesis of alkaline rocks explained by the addition of CO_2-rich components and/or recycled

690　crustal materials with or without sediment to the mantle (e.g., Dasgupta et al. 2007; Hofmann, 1997).

691　Conversely, the melting of an amphibole-rich metasomatic vein explains the major and trace element

composition of alkali basalts (Pilet et al., 2008; Pilet, 2015). However, the experimentally produced melts exhibit Pb depletion and a positive Nb-Ti anomaly in the PM-normalized trace element patterns (Fig. S8), which is inconsistent with the petit-spot basalts (Fig. 7). Moreover, Juriček and Keppler (2023) demonstrated that amphibole dehydration is not the cause for the oceanic LAB through high-pressure experiments under the realistic conditions. The fertile pyroxenitic xenoliths and pyroxene xenocrysts in the 1466R6 and R7 basalts, originating from the metasomatic vein related to prior petit-spot magmatism, had neither amphiboles nor other hydrous minerals (Mikuni et al., 2022).

To explore the involvement of carbonatitic and crustal components in petit-spot melts, a partial melting model of the heterogeneous mantle is presented. The involvement of carbonatitic fluids and recycled materials in the genesis of petit-spot melts has been suggested, and the open-system model with carbonatite influx from the outer system was employed using "OSM-4" by Ozawa (2001), and by referring the parameters by Borisova and Tilhac (2021). This model is based on the mass conservation equations of one-dimensional steady-state melting. In this study, the model asset the critical melt fraction (α_c; mass fraction of melt when melt separation begins = melt connectivity threshold) at 0.005 or 0.01. The system opens to fluxing at a constant melt-separation rate (γ) when the system reaches the α_c. The final trapped melt fraction (α_f; mass fraction of melt trapped in the residue) was fixed at ~0 (it was calculated as 10^{-6} owing to mass balance). We calculated the trace element composition of partial melts at various degrees of melting (F) as well as a few rates of influx (β) and melt separation (γ). We assumed a primitive mantle (PM) source as the lherzolite with or without a normal (N)-MORB source as the recycled oceanic crust (Sun and McDonough, 1989), such as pyroxenite and eclogite. The recycled crust (N-MORB component) was mixed in the source as compositional heterogeneity calculated as "0.05N-MORB + 0.95PM" for trace element concentration. The mineral phases and their proportions considered were derived only from garnet lherzolite (i.e., olivine, orthopyroxene, clinopyroxene, and garnet). The mineral mode of garnet lherzolite (olivine 55%, orthopyroxene 20%, clinopyroxene 15%, and garnet 10%) and the melting reaction mode (olivine 8%, orthopyroxene −19%, clinopyroxene 81%, and garnet 30%) are based on studies by Johnson et al. (1990) and Walter (1998), respectively. The proportion of olivine and garnet was also changed to assess the effect of the garnet modal ratio on the produced melt composition. In this situation, the clinopyroxene is consumed at a degree of partial melting of ~ 19%; hence, the system was calculated up to 18% partial melting. The carbonatite melt used in this model as a influx is "average carbonatite" from a study by Bizimis et al. (2003). The partition coefficient of trace elements is generally based on a study by McKenzie and O'Nions (1991, 1995), excluding Ti for clinopyroxene and garnet (Kelemen et al., 2003). The variables of β (influx rate) and γ (melt-separation rate) were changed during the modeling within the mass balance ($\gamma \leqq \beta + 1$). The modeled melts were outputted as "total melt," considering the instantaneous and accumulated melts. For the carbonatite composition, the value of "average carbonatite" from Bizimis et al. (2003) is applied because the chemical

composition of carbonatite is largely diverse, and this value is recommended for geochemical modeling (Bizimis et al., 2003). The parameters are detained in Table S6. Consequently, partial melting of garnet lherzolite with a 10% carbonatite influx to a given mass of source (i.e., garnet lherzolite) can provide a rough explanation of the trace element pattern of petit-spot basalts (Figs. 11a–e). The most plausible for petit-spot magma generation involves the presence of a 5% crustal component in the source (Figs. 11b and d). In addition, having slightly less garnet in the lherzolite source than the modal ratio of Johnson et al. (1990) offers a better fit for petit-spot characteristics (Fig. 11b). In both scenarios, incorporating a crustal component in the source produces more plausible outcomes (Figs. 11a–d). The higher carbonatite influx (β =1.0) could not explain the trace element composition of the petit-spot basalts (Fig. 11f). A melt connectivity threshold (α_c) of 0.01 is considered plausible, as higher connectivity of melt (i.e., lower α_c value) leads to enrichment of LILEs and LREEs (Fig. 11g). The results also indicate that the melt-separation ratio has no significant impact on the trace element composition of the calculated melts (Figs. 11d and e). Thereafter, we concluded that the partial melting of ~5% crustal component-bearing garnet lherzolite with ~10% carbonatite flux to a given mass of the source plausibly explains the melting source of petit-spot volcanoes (Figs. 11b and d). Assuming that the trace element composition of 1203, 1206, 1542, and 1544 basalts are also primitive, they could be explained by the partial melting of garnet lherzolite with 5% crustal component and lower carbonatite influx rate (β = 0.03) (Fig. S9). Actually, the 1203, 1206, 1542, and 1544 basalts exhibited similar MgO contents and Mg# to those of the 1522 basalts (Fig. 4 and Table 2). These results provide quantitative evidence regarding petit-spots' petrogenesis, i.e., the contribution of carbonatite melt and recycled oceanic crust.

Although the melting source included small proportions of carbonatite melt and crustal components, these components could have contributed to isotopic composition owing to their abundant incompatible elements, as opposed to the ambient mantle. Determination of the Sr, Nd, and Pb isotopic compositions indicated that they had geochemically identical prevalent mantle (PREMA)-like sources (Fig. 9). Contrary to those of NW Pacific petit-spots, which exhibit EM-1 isotopic composition (Machida et al., 2009; Liu et al., 2020), the samples herein did not align with any mantle isotopic endmembers (i.e., depleted MORB mantle (DMM); EM-1 and EM-2; and HIMU; Fig. 9). In the Pb isotopic space, the present samples did not correlate with those of the neighboring HIMU-like Cretaceous seamounts (Fig. 9a) (N-Wake, S-Wake seamounts; Konter et al., 2008; Koppers et al., 2003; Natland, 1976; Smith et al., 1989; Staudigel et al., 1991). For the melting source of the NW Pacific petit-spot basalts, the involvement of the eclogite/pyroxenite endmember as recycled oceanic crust and the carbonated endmember was suggested. This suggestion was based on the major and trace elements and the Mg, Sr, Nd, and Pb isotopic compositions with Mg diffusion modeling (Liu et al., 2020). The higher FeO/MnO ratios observed in the present melts (65.9–78.0), compared to those of partial melts originating from peridotite (50–60), are attributed to the presence of recycled pyroxenite

764   (Herzberg, 2011), potentially contributing to crustal components in the melting source. However, the

765   western Pacific petit-spots in this study uniformly displayed a PREMA-like isotopic signature without

766   extreme endmember contributions, as described previously (Fig. 9). Such isotopic compositions with

767   the world's petit-spots can be possibly explained by the diverse mixing proportion of HIMU and EM-

768   1 components (Fig. 9e). The isotopic compositions of the NW Pacific petit-spots (off the Japan Trench),

769   Samoan petit-spots (off the Tonga Trench), petit-spot dikes in Christmas Island (off the Java trench),

770   and western Pacific petit-spots (off the Mariana Trench in this study) are roughly along the HIMU–

771   EM-1 mixing line (Fig. 9e). Furthermore, the isotopic compositions of global carbonatites can

772   generally be explained by the mixing of HIMU and EM-1 (Bell and Tilton, 2002; Hoernle et al., 2002;

773   Hulett et al., 2016). The contributions of the carbonated material/carbonatite and crustal components

774   to the melting source were suggested in relation to the origin of HIMU and EM-1 (Collerson et al.,

775   2010; Hanyu et al., 2011; Wang et al., 2018; Weiss et al., 2016; Workman et al., 2004; Zindler and

776   Hart, 1986). However, the determination of EM-1 and HIMU components as carbonated components

777   and recycled crust, respectively, is challenging due to the varied perspectives on each tectonic setting

778   for the mantle endmember. The variability of global carbonatite isotopic compositions poses

779   challenges in determining their representative isotope ratios (Fig. 9). Despite these challenges

780   hindering a quantitative isotopic mixing model, the HIMU-EM-1-like trend observed in global petit-

781   spot volcanoes suggests the involvement of carbonatitic and recycled crustal materials. In conclusion,

782   the mass balance models applied to trace elements and the isotopic variations in the petit-spot

783   volcanoes confirmed the contribution of carbonatite melt and the recycled oceanic crust to the melting

784   source of the western Pacific petit-spots (Fig. 12). Experimental studies have revealed the diverse

785   petrogenesis scenarios of carbonatite and carbonatitic alkali-rich magma under high pressures

786   (Dasgupta et al., 2006; Ghosh et al., 2009). The geochemistry of petit-spot basalts including Mg

787   isotopes suggested that the conceivable origin of carbonatite related to the petit-spot melt is subducted

788   "carbonated" pelite, pyroxenite/eclogite, or peridotite stored as diamond or metal carbide in the

789   reduced lower portion of the upper mantle (Liu et al., 2020; Rohrbach et al., 2007). For instance,

790   subducted carbonated pelite would melt under high pressure (>8 GPa) through oxidation at the redox

791   boundary where the iron-wüstite (IW) buffer changes to the quartz–fayalite–magnetite (QFM) buffer

792   (i.e., redox melting; Grassi and Schmidt, 2011). Chen et al. (2022) demonstrated that the alkali-rich

793   carbonatite melt could occur at a pressure exceeding 6 GPa, particularly exhibiting K-rich and Na-rich

794   carbonatites under 6–12 and >12 GPa, respectively. This pressure-dependent alkalinity of the resulting

795   carbonatite melts could potentially account for the differences between potassic NW Pacific petit-spot

796   lavas and present sodic petit-spot lavas (Fig. 4b). On the other hand, an experimental study highlighted

797   the presence of a carbonate-rich layer in the LAB owing to the horizontally spread carbonate from

798   around the wedge mantle rather than upwelling from the deep mantle (Hammouda et al., 2020). Several

799   high pressure–temperature experiments and modeling revealed that the chemical composition of

800 intraplate magmas originating from the upper mantle depends on their original depth. Specifically, the

801 carbonatitic melt can be generated beneath thick cratonic lithosphere (~250–200 km), kimberlitic melt

802 could be produced at >120 km in depth, and alkali basalt could occur at 100–60-km depth by the

803 partial melting of "original" CO_2 and H_2O-bearing mantle (Massuyeau et al., 2021). This depth-

804 dependent variation in composition, i.e., K-rich kimberlite to alkali basalt, may provide an explanation

805 for the geochemical gap between K-rich NW Pacific petit-spots and K-poor western Pacific petit-spots

806 (Fig. 4b). Although the multiple origins of carbonatite are merely suggested and remain unclear,

807 carbon-rich components play a key role in the partial melting of mantle at the LAB (Sifré et al., 2014),

808 constituting the source of petit-spot magma.
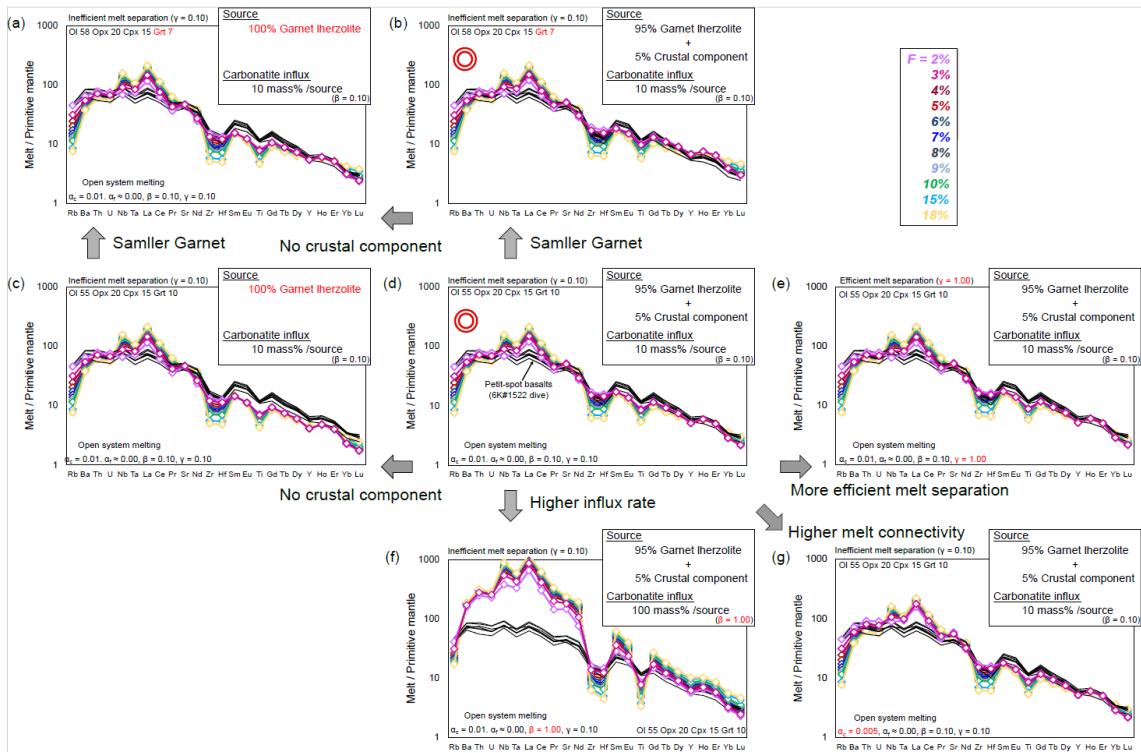
809

810 Fig. 11. Geochemical modeling for the primitive mantle (PM)-normalized trace-element pattern. The calculated

811   hypothetical melts are a production of carbonatite influx melting of garnet lherzolite with or without 5%

812   crustal component. Detailed information of the parameters is described in Section 6-3 and Table S6. F is

813   the degree of melting (%). The trace-element composition of the western Pacific petit-spot basalts from

814   the 6K#1522 dive is shown as black lines for comparison. The PM composition of lherzolite and the N-

815   MORB composition of recycled crust were based on a study by Sun and McDonough (1989). The influx

816   carbonatite is the "average carbonatite" of a study by Bizimis et al. (2003). The parameters used in the

817   open-system melting models were as follows: a_c is a critical melt fraction, a_f is a final trapped melt

818   fraction, β is a melt influx rate, and γ is a melt-separation rate. Model results are compared by varying

819   each parameter, i.e., garnet modal ratio and presence of crustal material (a–d), melt-separation rate (d and

820   e), carbonatite influx rate (d and f), and critical melt fraction (d and g). Each figure is expressed based on

32

821   the difference from the condition in (d).

822
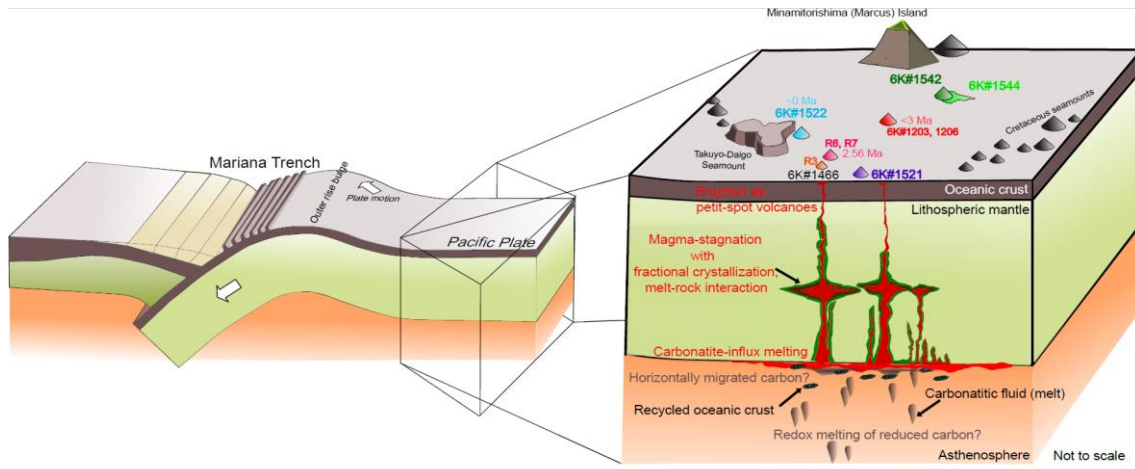
823

824 Fig. 12. Schematic illustration of the magmatic processes of the western Pacific petit-spot volcanoes.

825   Carbonatitic melt and recycled oceanic crust potentially induce partial melting of asthenospheric mantle

826   beneath the western Pacific region. Carbonatitic melt might have originated from a carbon-rich

827   component horizontally migrated from a subduction zone (Hammouda et al., 2020), or a redox melting

828   of reduced carbon in the deep mantle (Chen et al., 2022; Grassi and Schmidt, 2011; Rohrbach et al., 2007).

829   Petit-spot magma stagnated in the lithosphere with fractional crystallization and melt-rock interaction

830   (Mikuni et al., 2022), and they have erupted at ~0–3 Ma.

831

832 7 Conclusion

833

834   The occurrence of petit-spot volcanism supports partial melting at the LAB, carrying significant

835 implications for the characteristics of this geophysical discontinuity. Numerous instances of petit-spot

836 magmatism occurred on the western Pacific Plate at ~0–3 Ma, originating from similar PREMA-like

837 melting sources based on $^{40}Ar/^{39}Ar$ dating and the Sr, Nd, and Pb isotopic compositions. The mass

838 balance-based open-system modeling for trace elements revealed that the western Pacific petit-spot

839 magma was generated by the partial melting of a small amount (5%) of oceanic crust-bearing garnet

840 lherzolite with 3%–10% carbonatite influx to a given mass of the source. The isotopic compositions

841 of Sr, Nd, and Pb of the study samples, in conjunction with those of the NW Pacific petit-spots, petit-

842 spots off the Tonga and Java Trenches, could be explained by mixing the EM-1-like and HIMU-like

843 components, contributing to the subducted carbonated/crustal materials. The tectonic-induced

844 magmatism, such as a petit-spot, may follow a similar melting mechanism.

845

846 Authorship contributions

847

Competing Interests

Data availability

The data newly analyzed in this study and results of geochemical modeling are included in digital format in the online data repository of this paper (Tables 1, 2, 3 and 4, and Supplementary Tables S1 to S6).

Acknowledgement

References

886 Aftabuzzaman, M.R., Yomogoda, K., Suzuki, S., Takayanagi, H., Ishigaki, A., Machida, S., Asahara,
887   Y., Yamamoto, K., Hirano, N., Sano, S.-I., Chiyonobu, S., Bassi, D. and Iryu, Y.: Multi-
888   approach characterization of shallow-water carbonates off Minamitorishima and their
889   depositional settings/history, Island Arc, 30, e12400, https://doi.org/10.1111/iar.12400, 2021.
890 Akizawa, N., Ozawa, K., Tamura, A., Michibayashi, K. and Arai, S.: Three-dimensional evolution of
891   melting, heat and melt transfer in ascending mantle beneath a fast-spreading ridge segment
892   constrained by trace elements in clinopyroxene from concordant dunites and host
893   harzburgites of the Oman ophiolite, J. Petrol., 57, 777–814,
894   https://doi.org/10.1093/petrology/egw020, 2016.
895 Akizawa, N., Ohara, Y., Okino, K., Ishizuka, O., Yamashita, H., Machida, S., Sanfilippo, A., Basch,
896   V., Snow, J.E., Sen, A., Hirauchi, K.-I., Michibayashi, K., Harigane, Y., Fujii, M., Asanuma,
897   H. and Hirata, T.: Geochemical characteristics of back-arc basin lower crust and upper
898   mantle at final spreading stage of Shikoku Basin: an example of Mado Megamullion, Prog.
899   Earth Planet. Sci., 8, 65, https://doi.org/10.1186/s40645-021-00454-3, 2021.
900 Akizawa, N., Hirano, N., Matsuzaki, K.M., Machida, S., Tamura, C., Kaneko, J., Iwano, H.,
901   Danhara, T. and Hirata, T.: A direct evidence for disturbance of whole sediment layer in the
902   subducting Pacific plate by petit-spot magma–water/sediment interaction, Mar. Geol., 444,
903   106712, https://doi.org/10.1016/j.margeo.2021.106712, 2022.
904 Asimow, P. D. and Langmuir, C. H.: The importance of water to oceanic mantle melting regimes,
905   Nature, 421, 815–820, https://doi.org/10.1038/nature01429, 2003.
906 Audhkhasi, P. and Singh, S.C.: Discovery of distinct lithosphere-asthenosphere boundary and the
907   Gutenberg discontinuity in the Atlantic Ocean, Sci. Adv., 8, eabn5404,
908   https://doi.org/10.1126/sciadv.abn5404, 2022.
909 Axen G.J., van Wijk, J.W. and Currie, C.A.: Basal continental mantle lithosphere displaced by flat-
910   slab subduction, Nat. Geosci., 11, 961–964, https://doi.org/10.1038/s41561-018-0263-9,
911   2018.
912 Azami, K., Machida, S., Hirano, N., Nakamura, K., Yasukawa, K., Kogiso, T., Nakanishi, M. and
913   Kato, Y.: Hydrothermal ferromanganese oxides around a petit-spot volcano on old and cold
914   oceanic crust, Commun. Earth Environ., 4, 191, https://doi.org/10.1038/s43247-023-00832-
915   3, 2023.
916 Bell, K. and Tilton, G. R.: Probing the mantle: the story from carbonatites, Eos, 83, 273–277,
917   https://doi.org/10.1029/2002EO000190, 2002.
918 Bellas, A., Zhong, S. and Watts, A.B.: Reconciling lithospheric rheology between laboratory
919   experiments, field observations and different tectonic settings, Geophys. J. Int., 228, 857–
920   875, https://doi.org/10.1093/gji/ggab382, 2022.
921 Bianco, T.A, Ito, G., Becker, J.M. and Garcia, M.O.: Secondary Hawaiian volcanism formed by

922   flexural arch decompression, Geochem. Geophys. Geosyst. 6, Q08009,

923   https://doi.org/10.1029/2005GC000945, 2005.

924   Bizimis, M., Salters, V.J.M. and Dawson, J.B.: The brevity of carbonatite sources in the mantle:

925   evidence from Hf isotopes, Contrib. to Mineral. Petrol., 145, 281–300,

926   https://doi.org/0.1007/s00410-003-0452-3, 2003.

927   Bizimis, M., Salters, V.J.M., Garcia, M.O. and Norman, M.D.: The composition and distribution of

928   the rejuvenated component across the Hawaiian plume: Hf-Nd-Sr-Pb isotope systematics of

929   Kaula lavas and pyroxenite xenoliths, Geochem. Geophys. Geosyst. 14, 4458–4478,

930   https://doi.org/10.1002/ggge.20250, 2013.

931   Borsova, A.Y. and Tilhac, R.: Derivation of Hawaiian rejuvenated magmas from deep carbonated

932   mantle sources: A review of experimental and natural constraints, Earth. Sci. Rev., 222,

933   103819, https://doi.org/10.1016/j.earscirev.2021.103819, 2021.

934   Buchs, D.M., Pilet, S., Cosca, M., Flores, K.E., Bandini, A.N. and Baumgartner, P.O.: Low-volume

935   intraplate volcanism in the Early/Middle Jurassic Pacific basin documented by accreted

936   sequences in Costa Rica, Geochem. Geophys. Geosyst.,14, 1552–1568,

937   https://doi.org/10.1002/ggge.20084, 2013.

938   Chantel, J., Manthilake, G., Andrault, D., Novella, D., yu, T. and Wang, Y.: Experimental evidence

939   supports mantle partial melting in the asthenosphere, Sci. Adv., 2, e1600246,

940   https://doi.org/10.1126/sciadv.1600246, 2016.

941   Chen, X., Wang, M., Inoue, T., Liu, Q., Zhang, L. and Bader, T.: Melting of carbonated pelite at 5.5–

942   15.5 GPa: implications for the origin of alkali-rich carbonatites and the deep water and

943   carbon cycles, Contrib. to Mineral. Petrol., 177, 2, https://doi.org/10.1007/s00410-021-

944   01867-5, 2022.

945   Clague, D.A. and Frey, F.A.: Petrology and Trace element Geochemistry of the Honolulu Volcanics,

946   Oahu: Implications for the Oceanic Mantle below Hawaii, J, Petrol., 23, 447–504,

947   https://doi.org/10.1093/petrology/23.3.447, 1982.

948   Clague, D.A., Holcomb, R.T., Sinton, J.M., Detrick, R.S. and Torresan, M.E.: Pliocene and

949   Pleistocene alkali flood basalts on the seafloor north of the Hawaiian island, Earth Planet.

950   Sci. Lett., 98, 175–191, https://doi.org/10.1016/0012-821X(90)90058-6, 1990.

951   Clague, D.A., Moore, J.G.: The proximal part of the giant submarine Wailau landslide, Molokai,

952   Hawaii, J. Volcanol. Geotherm. Res., 113, 259–287, https://doi.org/10.1016/S0377-

953   0273(01)00261-X, 2002.

954   Collerson, K.D., Williams, Q., Ewart, A.E. and Murphy, D.T.: Origin of HIMU and EM-1 domains

955   sampled by ocean island basalts, kimberlites and carbonatites: The role of CO_2-fluxed lower

956   mantle melting in thermochemical upwellings, Phys. Earth Planet. Inter., 181, 112–131,

957   https://doi.org/10.1016/j.pepi.2010.05.008, 2010.

958   Conrad, C.P., Bianco, T.A., Smith, E.I. and Wessel, P.: Patterns of intraplate volcanism controlled by
959   asthenospheric shear. Nat. Geosci., 4, 317–321, https://doi.org/10.1038/ngeo1111, 2011.

960   Cousens, B.L. and Clague, D.A.: Shield to Rejuvenated Stage Volcanism on Kauai and Niihau,
961   Hawaiian Islands, J. Petrol., 56, 1547–1584, https://doi.org/10.1093/petrology/egv045,
962   2015.

963   Dasgupta, R. and Hirschmann, M.M.: Melting in the Earth's deep upper mantle caused by carbon
964   dioxide, Nature, 440, 659–662, https://doi.org/10.1038/nature04612, 2006.

965   Dasgupta, R., Hirschmann, M.M. and Stalker, K.: Immiscible Transition from Carbonate-rich to
966   Silicate-rich Melts in the 3 GPa Melting Interval of Eclogite + CO2 and Genesis of Silica-
967   undersaturated Ocean Island Lavas, J. Petrol., 47, 647–671,
968   https://doi.org/10.1093/petrology/egi088, 2006.

969   Dasgupta, R., Hirschmann, M.M. and Smith, N.D.: Partial Melting Experiments of Peridotite + CO2
970   at 3 GPa and Genesis of Alkalic Ocean Island Basalts, J. Petrol., 48, 2093–2124,
971   https://doi.org/10.1093/petrology/egm053, 2007.

972   Dasgupta, R., Hirschmann, M.M., McDonough, W.F., Spiegelman, M. and Withers, A.: Trace
973   element partitioning between garnet lherzolite and carbonatite at 6.6 and 8.6 GPa with
974   applications to the geochemistry of the mantle and of mantle-derived melts, Chem. Geol.,
975   262, 57–77, https://doi.org/10.1016/j.chemgeo.2009.02.004, 2009.

976   Dasgupta, R., Mallik, A., Tsuno, K., Withers, A.C., Hirth, G. and Hirschmann, M.M.: Carbon-
977   dioxide-rich silicate melt in the Earth's upper mantle, Nature, 493, 211–215,
978   https://doi.org/10.1038/nature11731, 2013.

979   Debayle, E., Bodin, T., Durand, S. and Ricard, Y.: Seismic evidence for partial melt below tectonic
980   plates, Nature, 586, 555–559, https://doi.org/10.1038/s41586-020-2809-4, 2020.

981   Dixon, J., Clague, D.A., Cousens, B., Monsalve, M.L. and Uhl, J.: Carbonatite and silicate melt
982   metasomatism of the mantle surrounding the Hawaiian plume: evidence from volatiles, trace
983   elements, and radiogenic isotopes in rejuvenated-stage lavas from Niihau, Hawaii,
984   Geochem. Geophys. Geosyst., 9, Q09005, https://doi.org/10.1029/2008GC002076, 2008.

985   Ebisawa, N., Sumino, H., Okazaki, R., Takigami, Y., Hirano, N., Nagao, K. and Kaneoka, I.:
986   Construction of I-Xe and ^{40}Ar–^{39}Ar dating system using a modified VG3600 noble gas mass
987   spectrometer and the first I-Xe data obtained in Japan, J. Mass Spectrom. Soc. Jpn., 52,
988   219–229, https://doi.org/10.5702/massspec.52.219, 2004.

989   Falloon, T. J. and Green, D. H.: The solidus of carbonated, fertile peridotite. Earth Planet. Sci. Lett.
990   94, 364–370, https://doi.org/10.1016/0012-821X(89)90153-2, 1989.

991   Falloon, T. J. and Green, D. H.: Solidus of carbonated fertile peridotite under fluid-saturated
992   conditions. Geology, 18, 195–199, https://doi.org/10.1130/0091-
993   7613(1990)018<0195:SOCFPU>2.3.CO;2, 1990.

994   Falloon, T.J. Hoernle, K., Schaefer, B.F., Bindeman, I.N., Hart, S.R., Garbe-Schonberg, D. and

995   Duncan, R.A.: Petrogenesis of Lava from Christmas Island, Northeast Indian Ocean:

996   Implications for the Nature of Recycled Components in Non-Plume Intraplate Settings,

997   Geosci., 12, 118, https://doi.org/10.3390/geosciences12030118, 2022.

998   Frey, F.A., Green, D.H. and Roy, S.D.: Integrated Models of Basalt Petrogenesis: A Study of Quartz

999   Tholeiites to Olivine Melilitites from South Eastern Australia Utilizing Geochemical and

1000   Experimental Petrological Data, J. Petrol., 19, 463–513,

1001   https://doi.org/10.1093/PETROLOGY/19.3.463, 1978.

1002   Frey, F.A., Clague, D., Mahoney, J.J. and Sinton, J.M.: Volcanism at the edge of the Hawaiian

1003   plume: Petrogenesis of submarine alkali lavas from the North Arch volcanic field, J. Petrol.,

1004   41, 667–691, https://doi.org/10.1093/petrology/41.5.667, 2000.

1005   Foley, S. F., Yaxley, G. M., Rosenthal, A., Buhre, S., Kiseeva, E. S., Rapp, R. P. and Jacob, D. E.:

1006   The composition of near-solidus melts of peridotite in the presence of CO_2 and H_2O

1007   between 40 and 60 kbar. Lithos, 112, 274–283, https://doi.org/10.1016/j.lithos.2009.03.020,

1008   2009.

1009   Fujie, G., Kodaira, S., Nakamura, Y., Morgan, J.P. Dannowski, A., Thorwart, M., Grevemeyer, I. and

1010   Miura, S.: Spatial variations of incoming sediments at the northeastern Japan arc and their

1011   implications for megathrust earthquakes, Geology, 48, 614–619,

1012   https://doi.org/10.1130/G46757.1, 2020.

1013   Fujiwara, T., Hirano, N. Abe, N. and Takizawa, K.: Subsurface structure of the "petit-spot"

1014   volcanoes on the northwestern Pacific Plate, Geophys. Res. Lett., 34, L13305,

1015   https://doi.org/10.1029/2007GL030439, 2007.

1016   Garcia, M.O., Weis, D., Jicha, B.R., Ito, G. and Hanano, D.: Petrology and geochronology of lavas

1017   from Ka'ula Volcano: Implications for rejuvenated volcanism of the Hawaiian mantle

1018   plume, Geochim. Cosmochim. Acta., 185, 278–301,

1019   https://doi.org/10.1016/j.gca.2016.03.025, 2016.

1020   Ghosh, S., Ohtani, E., Litasov, K.K. and Terasaki, H.: Solidus of carbonated peridotite from 10 to 20

1021   GPa and origin of magnesiocarbonatite melt in the Earth's deep mantle, Chem. Geol., 262,

1022   17–28, https://doi.org/10.1016/j.chemgeo.2008.12.030, 2009.

1023   Grassi, D. and Schmidt, M.W.: The Melting of Carbonated Pelites from 70 to 700 km Depth, J.

1024   Petrol., 52, 765–789, https://doi.org/10.1093/petrology/egr002, 2011.

1025   Gripp, A.E. and Gordon, R.G.: Current plate velocities relative to the hotspots incorporating the

1026   NUVEL-1 global plate motion model, Geophys. Res. Lett., 17, 1109–1112,

1027   https://doi.org/10.1029/GL017i008p01109, 1990.

1028   Hammouda, T., Manthilake, G., Goncalves, P., Chantel, J., Guignard, J., Crichton, W. and Gaillard,

1029   F.: Is There a Global Carbonate Layer in the Oceanic Mantle?, Geophys. Res. Lett., 48,

1030   e2020GL089752, https://doi.org/10.1029/2020GL089752, 2020.

1031 Hanano, D., Scoates, J.S. and Weis, D: Alteration mineralogy and the effect of acid-leaching on the

1032   Pb-isotope systematics of ocean-island basalts, Am. Mineral., 94, 17–26,

1033   https://doi.org/10.2138/am.2009.2845, 2009.

1034 Hanyu, T., Tatsumi, Y., Senda, R., Miyazaki, T., Chang, Q., Hirahara, Y., Takahashi, T., Kawabata,

1035   H., Suzuki, K., Kimura, J-I. and Nakai, S.: Geochemical characteristics and origin of the

1036   HIMU reservoir: A possible mantle plume source in the lower mantle, Geochem. Geophys.

1037   Geosyst., 12, Q0AC09, https://doi.org/10.1029/2010GC003252, 2011.

1038 Hanyu, T., Shimizu, K., Ushikubo, T., Kimura, J.-I., Chang, Q., Hamada, M., Ito, M., Iwamori, H.

1039   and Ishikawa, T.: Tiny droplets of ocean island basalts unveil Earth's deep chlorine cycle,

1040   Nat. Commun., 10, 60, https://doi.org/10.1038/s41467-018-07955-8, 2019.

1041 Hart, S.R.: A large-scale isotope anomaly in the Southern Hemisphere mantle, Nature, 309, 753–757,

1042   https://doi.org/10.1038/309753a0, 1984.

1043 Hart, S.R., Gerlach, D.C. and White, W.M.: A Possible new Sr-Nd-Pb mantle array and consequences

1044   for mantle mixing, Geochim. Cosmochim. Acta., 50, 1551–1557,

1045   https://doi.org/10.1016/0016-7037(86)90329-7, 1986.

1046 Hein, J.R., Koschinsky, A., Bau, M., Manheim, F.T., Kang, J.K. and Roberts, L.: Cobalt-rich

1047   ferromanganese crusts in the Pacific, Handbook of Marine Mineral Deposits (Cronan DS,

1048   ed.), 239–279, CRC Press, Boca Raton, Florida, 1999.

1049 Helz, R.T. and Thronber, C.R.: Geochemistry if Kilauea Iki lava lake, Hawaii, Bull. Volcanol., 49,

1050   651–658, https://doi.org/10.1007/BF01080357, 1987.

1051 Herath, P., Stern, T.A., Savage, M.K., Bassett, D. and Henrys, S.: Wide-angle seismic reflections

1052   reveal a lithosphere-asthenosphere boundary zone in the subducting Pacific Plate, New

1053   Zealand, Sci. Adv., 8, eabn5697, https://doi.org/10.1126/sciadv.abn5697, 2022.

1054 Herzberg, C.: Petrology and thermal structure of the Hawaiian plume from Mauna Kea volcano,

1055   Nature, 444, 605–609. https://doi.org/10.1038/nature05254, 2006.

1056 Herzberg, C.: Identification of Source Lithology in the Hawaiian and Canary Islands: Implications

1057   for Origins, J. Petrol., 52, 113–146, https://doi.org/10.1093/petrology/egq075, 2011.

1058 Hirano, N., Takahashi, E., Yamamoto, J., Abe, N., Ingle, S.P., Kaneoka, I., Hirata, T., Kimura, J.-I.,

1059   Ishii, T., Ogawa, Y., Machida, S. and Suyehiro, K.: Volcanism in response to plate flexure.

1060   Science, 313, 1426–1428. https://doi.org/10.1126/science.1128235, 2006.

1061 Hirano, N.: Petit-spot volcanism: a new type of volcanic zone discovered near a trench, Geochem. J.,

1062   45, 157–167, https://doi.org/10.2343/geochemj.1.0111, 2011.

1063 Hirano, N., Machida, S., Abe, N., Morishita, T., Tamura, A. and Arai, S.: Petit-spot lava fields off the

1064   central Chile trench induced by plate flexure, Geochem. J., 47, 249–257,

1065   https://doi.org/10.2343/geochemj.2.0227, 2013.

1066 Hirano, N., Nakanishi, M., Abe, N. and Machida, S.: Submarine lava fields in French Polynesia,
1067   Mar. Geol., 373, 39–48, http://dx.doi.org/10.1016/j.margeo.2016.01.002, 2016.

1068 Hirano, N., Machida, S., Sumino, H., Shimizu, K., Tamura, A., Morishita, T., Iwano, H., Sakata, S.,
1069   Ishii, T., Arai, S., Yoneda, S., Danhara, T. and Hirata, T.: Petit-spot volcanoes on the oldest
1070   portion of the Pacific Plate, Deep Sea Res. Part I, 154, 103142,
1071   https://doi.org/10.1016/j.dsr.2019.103142, 2019.

1072 Hirano, N., Sumino, H., Morishita, T., Machida, S., Kawano, T., Yasukawa, K., Hirata, T., Kato, Y.
1073   and Ishii, T.: A Paleogene magmatic overprint on Cretaceous seamounts of the western
1074   Pacific, Island Arc, 30, e12386, https://doi.org/10.1111/iar.12386, 2021.

1075 Hirano, N. and Machida, S.: The mantle structure below petit-spot volcanoes, Commun. Earth
1076   Environ., 3, 110, https://doi.org/10.1038/s43247-022-00438-1, 2022.

1077 Hirth, G. and Kohlstedt, D.L.: Water in the oceanic upper mantle: implications for rheology, melt
1078   extraction and the evolution of the lithosphere. Earth Planet. Sci. Lett., 144, 93–108,
1079   https://doi.org/10.1016/0012-821X(96)00154-9, 1996.

1080 Hoernle, K., Tilton, G., Le Bas, M.J., Duggem, S. and Garbe-Schönberg, D.: Geochemistry of
1081   oceanic carbonatites compared with continental carbonatites: mantle recycling of oceanic
1082   crustal carbonate, Contrib. to Mineral. Petrol., 142, 520–542,
1083   https://doi.org/10.1007/s004100100308, 2002.

1084 Hofmann, A.W.: Mantle geochemistry: the message from oceanic volcanism, Nature, 385, 219–229,
1085   https://doi.org/10.1038/385219a0, 1997.

1086 Hofmann, A.W.: Sampling mantle heterogeneity through oceanic basalts: isotopes and trace
1087   elements. In: Carson, R. W. (Ed.), Treatise on Geochemistry, 2, The Mantle and Core,
1088   Elsevier, 61–101, https://doi.org/10.1016/B0-08-043751-6/02123-X, 2003.

1089 Hosseini, K., Matthews, K.J., Sigloch, K., Shephard, G.E., Domeier, M. and Tsekhmistrenko, M.:
1090   SubMachine: Web-Based tools for exploring seismic tomography and other models of
1091   Earth's deep interior, Geochem. Geophys. Geosyst., 19, 1464–1483,
1092   https://doi.org/10.1029/2018GC007431, 2018.

1093 Hua, J., Fisher, K. M., Becker, T.W., Gazel, E. and Hirth, G.: Asthenospheric low-velocity zone
1094   consistent with globally prevalent partial melting, Nat. Geosci., 16, 175–181,
1095   https://doi.org/10.1038/s41561-022-01116-9, 2023.

1096 Hulett, S.R., Simonetti, A., Rasbury, E.T. and Hemming, N.G.: Recycling of subducted crustal
1097   components into carbonatite melts revealed by boron isotopes, Nat. Geosci., 9, 904–908,
1098   https://doi.org/10.1038/ngeo2831, 2016.

1099 Irvine, T. N. and Baragar, W. R. A.: A Guide to the Chemical Classification of the Common Volcanic
1100   Rocks, Can. J. Earth Sci., 8, 523–548, https://doi.org/10.1139/e71-055, 1971.

1101 Irving, A.J and Green, D.H.: Geochemistry and petrogenesis of the newer basalts of Victoria and

1102　　　　　South Australia, J. Geol. Sci. Australia., 23, 45–66,

1103　　　　　　　https://doi.org/10.1080/00167617608728920, 1976.

1104　Iwata, N.: Geochronological study of the Deccan volcanism by the ^{40}Ar–^{39}Ar method, Doctor

1105　　　　　　　Thesis, University of Tokyo, pp. 168, 1998.

1106　Jochum, K.P. and Nohl, U.: Reference materials in geochemistry and environmental research and the

1107　　　　　　　GeoReM database, Chem. Geol., 253, 50–53,

1108　　　　　　　https://doi.org/10.1016/j.chemgeo.2008.04.002, 2008.

1109　Johnson, K.T.M., Dick, H.J.B. and Shimizu, N.: Melting in the oceanic upper mantle: An ion

1110　　　　　　　microprobe study of diopsides in abyssal peridotites, J. Geophys. Res., 95, 2661–2678,

1111　　　　　　　https://doi.org/10.1029/JB095iB03p02661, 1990.

1112　Juriček, M.P and Keppler, H.: Amphibole stability, water storage in the mantle, and the nature of the

1113　　　　　　　lithosphere-asthenosphere boundary, Earth Planet. Sci. Lett., 608, 118082,

1114　　　　　　　https://doi.org/10.1016/j.epsl.2023.118082, 2023.

1115　Kaneko, J., Machida, S., Hirano, N., Kasaya, T. and Kumagai, H.: Near bottom MBES survey

1116　　　　　　　mounted on a HOV at 5500m depth. Oceans Conference Record (IEEE) 2022, 1–5,

1117　　　　　　　https://doi.org/10.1109/OCEANSChennai45887.2022.9775366, 2022.

1118　Kang, L. and Karato, S. -I.: Hydrogen Partitioning Between Olivine and Orthopyroxene:

1119　　　　　　　Implications for the Lithosphere-Asthenosphere Structure, J. Geophys. Res., 128,

1120　　　　　　　e2022JB025259, https://doi.org/10.1029/2022JB025259, 2023.

1121　Karato, S.-I. and Jung, H.: Water, partial melting and the origin of the seismic low velocity and high

1122　　　　　　　attenuation zone in the upper mantle, Earth Planet. Sci. Lett., 157, 193–207,

1123　　　　　　　https://doi.org/10.1016/S0012-821X(98)00034-X, 1998.

1124　Katsura, T. and Fei, H.: Asthenosphere dynamics based on the H_2O dependence of element

1125　　　　　　　diffusivity in olivine, Natl. Sci. Rev., 8, nwaa278. https://doi.org/10.1093/nsr/nwaa278,

1126　　　　　　　2021.

1127　Kawakatsu, H., Kumar, P., Takei, Y., Shinohara, M., Kanazawa, T., Araki, E. and Suyehiro, K.:

1128　　　　　　　Seismic Evidence for Sharp Lithosphere-Asthenosphere Boundaries of Oceanic Plates,

1129　　　　　　　Science, 324, 499–502, https://www.science.org/doi/10.1126/science.1169499, 2009.

1130　Kelemen, P.B., Yogodzinskim G.M., and Scholl, D.W.: Along-strike variation in the Aleutian Island

1131　　　　　　　Arc: genesis of high Mg# andesite and implications for continental crust, In: Eiler, J. (ed.),

1132　　　　　　　Inside the subduction Factory, American Geophysical Union, Geophysical Monograph, 138,

1133　　　　　　　223–276, https://doi.org/10.1029/138GM11, 2003.

1134　Keshav, S. and Gudfinnsson, G.H.: Silicate liquid-carbonatite liquid transition along the melting curve

1135　　　　　　　of model, vapor-saturated peridotite in the system $CaO-MgO-Al_2O_3-SiO_2-CO_2$ from 1.1 to

1136　　　　　　　2 GPa, J. Geophys. Res., 118, 3341–3353, https://doi.org/10.1002/jgrb.50249, 2013.

1137 Kiseeva, E.S., Litasov, K.D., Yaxley, G.M., Ohtani, E. and Kamenetsky, V.S.: Melting and Phase
1138   Relations of Carbonated Eclogite at 9–21 GPa and the Petrogenesis of Alkali-Rich Melts in
1139   the Deep Mantle, J. Petrol., 54, 1555–1583, https://doi.org/10.1093/petrology/egt023, 2013.

1140 Kobayashi, M., Sumino, H., Saito, T., Nagao, K.: Determination of halogens in geological reference
1141   materials using neutron irradiation noble gas mass spectrometry, Chem. Geol., 582, 120420,
1142   https://doi.org/10.1016/j.chemgeo.2021.120420, 2021.

1143 Konovalov, Y. I. and Martynov, Y. A.: Volcanic complex of the La Mont Guyot; Marcus-Wake Uplift,
1144   Pacific Ocean, Pacific Geology, 5, 40–47, 1992.

1145 Konter, J.G., Hanan, B.B., Blicher-Toft, J., Koppers, A.A.P., Plank, T. and Staudigel, H.: One
1146   hundred million years of mantle geochemical history suggest the retiring of mantle plumes
1147   is premature, Earth Planet Sci Lett, 275, 285–295,
1148   https://doi.org/10.1016/j.epsl.2008.08.023, 2008.

1149 Koppers, A. A. P., H. Staudigel. and J. R. Wijbrans.: Dating crystalline groundmass separates of
1150   altered Cretaceous seamount basalts by the Ar^{40}/Ar^{39} incremental heating technique, Chem.
1151   Geol., 166, 139–158. https://doi.org/10.1016/S0009-2541(99)00188-6, 2000.

1152 Koppers, A.A.P., Staudigel, H., Pringle, M.S. and Wijbrans, J.R.: Short-lived and discontinuous
1153   intra-plate volcanism in the South Pacific: hotspots or extensional volcanism?, Geochem.
1154   Geophys. Geosyst., 4, 1089, https://doi.org/10.1029/2003GC000533, 2003.

1155 Korenaga, J.: Plate tectonics and surface environment: Role of the oceanic upper mantle, Earth Sci.
1156   Rev., 205, 103185, https://doi.org/10.1016/j.earscirev.2020.103185, 2020.

1157 Le Bas, M. J., Le Maitre, R., Strackeisen, A. and Zanettin, B.: A chemical classification of volcanic
1158   rocks based on the total alkali–silica diagram, J. Petrol., 27, 745–750,
1159   https://doi.org/10.1093/petrology/27.3.745, 1986.

1160 Lu, C., Grand, S. P., Lai, H. and Garnero, E. J.: TX2019slab: A New P and S Tomography Model
1161   Incorporating Subducting Slabs, J. Geophys. Res., 124, 11549–11567,
1162   https://doi.org/10.1029/2019JB017448, 2019.

1163 Liu, J., Hirano, N., Machida, S., Xia, Q., Tao, C., Liao, S., Liang, J., Li W., Yang, W. Zhang, G. and
1164   Ding, T.: Melting of recycled ancient crust responsible for the Gutenberg discontinuity, Nat.
1165   Commun., 11, 172, https://doi.org/10.1038/s41467-019-13958-w, 2020.

1166 Longerich, H.P., Jackson, S.E. and Gunther, D.: Laser ablation inductively coupled plasma mass
1167   spectrometric transient signal data acquisition and analyte concentration calculation, J. Anal.
1168   At. Spectrom., 11, 899–904, https://doi.org/10.1039/ja9961100899, 1996.

1169 Machida, S., Hirano, N., and Kimura, J.-I.: Evidence for recycled material in Pacific upper mantle
1170   unrelated to plumes, Geochim. Cosmochim. Acta., 73, 3028–3037,
1171   http://dx.doi.org/10.1016/j.gca.2009.01.026, 2009.

1172 Machida, S., Orihashi, Y., Magnani, M., Neo, N., Wilson, S., Tanimizu, M., Yoneda, S., Yasuda, A.

1173   and Tamaki, K.: Regional mantle heterogeneity regulates melt production along the Réunion

1174   hotspot-influenced Central Indian Ridge, Geochem. J., 48, 433–449,

1175   https://doi.org/10.2343/geochemj.2.0320, 2014.

1176 Machida, S., Hirano, N., Sumino, H., Hirata, T., Yoneda, S. and Kato, Y: Petit-spot geology reveals

1177   melts in upper-most asthenosphere dragged by lithosphere, Earth Planet. Sci. Lett., 426,

1178   267–279, https://doi.org/10.1016/j.epsl.2015.06.018, 2015

1179 Machida, S., Fujinaga, K., Ishii, T., Nakamura, K., Hirano, N. and Kato, Y.: Geology and

1180   geochemistry of ferromanganese nodules in the Japanese Exclusive Economic Zone around

1181   Minamitorishima Island, Geochem. J., 50, 539–555,

1182   https://doi.org/10.2343/geochemj.2.0419, 2016.

1183 Machida, S., Kogiso, T. and Hirano, N.: Petit-spot as definitive evidence for partial melting in the

1184   asthenosphere caused by CO_2, Nat. Commun., 8, 14302,

1185   https://doi.org/10.1038/ncomms14302, 2017.

1186 Massuyeau, M., Gardés, E., Morizet, Y. and Gaillard, F.: A model for the activity of silica along the

1187   carbonatite–kimberlite–mellilitite–basanite melt compositional joint, Chem. Geol., 418,

1188   206–216, https://doi.org/10.1016/j.chemgeo.2015.07.025, 2015.

1189 Massuyeau, M., Gardés, E., Rogerie, G., Aulbach, S., Tappe, S., Le Trong, E., Sifré, D. and Gaillaer,

1190   F.: MAGLAB: A computing platform connecting geophysical signatures to melting

1191   processes in Earth's mantle, Phys. Earth Planet., 314, 106638,

1192   https://doi.org/10.1016/j.pepi.2020.106638, 2021.

1193 McKenzie, D. and O'Nions, R.K.: Partial melt distributions from inversion of rare Earth element

1194   concentrations, J. Petrol., 32, 1021–1091, https://doi.org/10.1093/petrology/32.5.1021,

1195   1991.

1196 McKenzie, D. and O'Nions, R.K.: The Source Regions of Ocean Island Basalts, J. Petrol., 36, 133–

1197   159, https://doi.org/10.1093/petrology/36.1.133, 1995.

1198 Melson, W.G., Thompson, G. and van Andel, T.H.: Volcanism and metamorphism in the Mid-

1199   Atlantic Ridge, 22°N latitude, J. Geophys. Res., 73, 5925–5941,

1200   https://doi.org/10.1029/JB073i018p05925, 1968.

1201 Mierdel, K., Keppler, H., Smyth, J.R. and Langenhorst, F.: Water solubility in aluminous

1202   orthopyroxene and the origin of Earth's Asthenosphere, Science, 315, 364–368,

1203   https://doi.org/10.1126/science.1135422, 2007.

1204 Mikuni, K., Hirano, N., Akizawa, N., Yamamoto, J., Machida, S., Tamura, A., Hagiwara, Y.,

1205   Morishita, T.: Lithological structure of western Pacific lithosphere reconstructed from

1206   mantle xenoliths in a petit-spot volcano, Prog. Earth Planet. Sci., 9, 62,

1207   https://doi.org/10.1186/s40645-022-00518-y, 2022.

1208 Miyashiro, A., Shido, F. and Ewing, M.: Metamorphism on the Mid-Atlantic Ridge near 24 and 30°

1209   N. Phil. Trans. Roy. Soc. Lond., 268, 589–603, https://doi.org/10.1098/rsta.1971.0014,

1210   1971.

1211 Morimoto, N.: Nomenclature of pyroxenes. Mineral. Petrol., 39, 55–76,

1212   https://doi.org/10.1007/BF01226262, 1988.

1213 Moore, J.G., Fornari, D.J. and Clague, D.A.: Basalts from the 1877 Submarine Eruption of Mauna

1214   Loa, Hawaii; New Data on the Variation of Palagonitization Rate with Temperature. United

1215   States Geol. Surv. Bull. 1663., 1–11, https://doi.org/10.3133/b1663, 1985.

1216 Müller, R.D., Sdrolias, M., Gaina, C. and Roest, W.R.: Age, spreading rates, and spreading

1217   asymmetry of the world's ocean crust. Geochem. Geophys. Geosyst., 9, Q04006.

1218   http://dx.doi.org/10.1029/2007GC001743, 2008.

1219 Natland, J.: Petrology of Volcanic Rocks Dredged from Seamounts in the Line Islands, Init. Rep.

1220   Deep Sea Drill. Proj., 33, 749–777. https://doi.org/10.2973/dsdp.proc.33.126.1976, 1976.

1221 Nier, A.: A redetermination of the relative abundances of the isotopes of carbon, nitrogen, oxygen,

1222   argon, and potassium, Phys. Rev., 77, 789-793, https://doi.org/10.1103/PhysRev.77.789,

1223   1950.

1224 Nobre Silva, I.G., Weis, D., Barling, J. and Scoates, J.S.: Leaching systematics and matrix

1225   elimination for the determination of high-precision Pb isotope compositions of ocean island

1226   basalts, Geochem. Geophys. Geosyst., 10, Q08012, https://doi.org/10.1029/2009GC002537,

1227   2009.

1228 Novella, D., Keshav, S., Gudfinnsson, G.H. and Ghosh, S.: Melting phase relations of model

1229   carbonated peridotite from 2 to 3 GPa in the system $CaO-MgO-Al_2O_3-SiO_2-CO_2$ and further

1230   indication of possible unmixing between carbonatite and silicate liquids, J. Geophys. Res.,

1231   119, 2780–2800, https://doi.org/10.1002/2013JB010913, 2014.

1232 Nozaki, T., Tokumaru, A., Takaya, Y., Kato, Y., Suzuki, K. and Urabe, T.: Major and trace element

1233   compositions and resource potential of ferromanganese crust at Takuyo Daigo Seamount,

1234   northwestern Pacific Ocean, Geochem J, 50, 527–537,

1235   https://doi.org/10.2343/geochemj.2.0430, 2016.

1236 Okumura, S. and Hirano, N.: Carbon dioxide emission to earth's surface by deep-sea volcanism,

1237   Geology, 41, 1167–1170, https://doi.org/10.1130/G34620.1, 2013.

1238 Orihashi, Y., Maeda, J., Tanaka, R., Zeniya, R. and Niida, K.: Sr and Nd isotopic data for the seven

1239   GSJ rock reference samples; JA-1, JB-1a, JB-2, JB-3, JG-1a, JGb-1 and JR-1, Geochem. J.,

1240   32, 205–211, https://doi.org/10.2343/geochemj.32.205, 1998.

1241 Ozawa, K.: Mass balance equations for open magmatic systems: Trace element behavior and its

1242   application to open system melting in the upper mantle. J. Geophys. Res., 106, 13407–

1243   13434, https://doi.org/10.1029/2001JB900001, 2001.

1244 Pearce, N.J.G., Perkins, W.T., Westgate, J.A., Gorton, M.P., Jackson, S.E., Neal, C.R. and Chenery,

1245   S.P.: A compilation of new and published major and trace element data for NIST SRM 610

1246   and NIST SRM 612 glass reference materials, Geostand. Newsl., 21, 115–144,

1247   https://doi.org/10.1111/j.1751-908X.1997.tb00538.x, 1997.

1248 Pilet, S., Baker, M.B. and Stolper, E.M.: Metasomatized Lithosphere and the Origin of Alkaline

1249   Lavas, Science, 320, 916–919, https://doi.org/10.1126/science.1156, 2008.

1250 Pilet, S.: Generation of low-silica alkaline lavas: Petrological constrains, models, and thermal

1251   implications, The Interdisciplinary Earth: A Volume in Honor of Don L. Anderson, Gillian

1252   R. Foulger, Michele Lustrino, Scott D. King. https://doi.org/10.1130/2015.2514(17), 2015.

1253 Pilet, S., Abe, N., Rochat, L., Kaczmarek, M.-A., Hirano, N., Machida, S., Buchs, D.M.,

1254   Baumgarther, P.O. and Müntener, O.: Pre-subduction metasomatic enrichment of the oceanic

1255   lithosphere induced by plate flexure, Nat. Geosci., 9, 898–903,

1256   https://doi.org/10.1038/ngeo2825, 2016.

1257 Regelous, M., Weinzierl, C.G. and Haase, K.M.: Controls on melting at spreading ridges from

1258   correlated abyssal peridotite – mid-ocean ridge basalt compositions, Earth Planet. Sci. Lett.,

1259   449, 1–11. http://dx.doi.org/10.1016/j.epsl.2016.05.017, 2016.

1260 Reinhard, A.A., Jackson, M.G., Blusztajn, J., Koppers, A.A.P., Simms, A.R. and Konter, J.G.: "Petit

1261   Spot" Rejuvenated Volcanism Superimposed on Plume-Derived Samoan Shield Volcanoes:

1262   Evidence From a 645-m Drill Core From Tutuila Island, American Samoa, Geochem.

1263   Geophys. Geosys., 20, 1485–1507, https://doi.org/10.1029/2018GC007985, 2019.

1264 Resing, J.A. and Sansone, F.J.: The chemistry of lava–seawater interactions: the generation of

1265   acidity, Geochim. Cosmochim. Acta., 63, 2183–2198, https://doi.org/10.1016/S0016-

1266   7037(99)00193-3, 1999.

1267 Rohrbach, A., Ballhaus, C., Golla-Schindler, U., Ulmer, P., Kamenetsky, V.S. and Kuzmin, D.V.:

1268   Metal saturation in the upper mantle, Nature, 449, 456–458,

1269   https://doi.org/10.1038/nature06183, 2007.

1270 Rychert, C. A. and Shearer, P. M.: A global view of the lithosphere–asthenosphere boundary,

1271   Science, 324, 495–498, https://www.science.org/doi/10.1126/science.1169754, 2009.

1272 Sakamaki, T., Suzuki, A., Ohtani, E., Terasaki, H., urakawa, S., Katayama, Y., Funakoshi, K.-I.,

1273   Wang, Y. Hernlund, J.H. and Ballmer, M.D.: Ponded melt at the boundary between the

1274   lithosphere and asthenosphere, Nat. Geosci., 6, 1041–1044,

1275   https://doi.org/10.1038/ngeo1982, 2013.

1276 Shaw, D.M.: Trace element fractionation during anataxis, Geochim. Cosmochim. Acta., 34, 237–

1277   243, https://doi.org/10.1016/0016-7037(70)90009-8, 1970.

1278 Shaw, C.S.J.: Dissolution of orthopyroxene in basanitic magma between 0.4 and 2 GPa: Further

1279   implications for the origin of Si–rich alkaline glass inclusions in mantle xenoliths, Contrib.

1280   Mineral. Petrol., 135, 114–132, https://doi.org/10.1007/s004100050501, 1999.

1281 Sifré, D., Gardés, E., Massuyeau, M., Hashim, L., Hier-Majumder, S. and Gaillard, F.: Electrical
1282   conductivity during incipient melting in the oceanic low-velocity zone, Nature, 509, 81–85,
1283   https://doi.org/10.1038/nature13245, 2014.

1284 Smith, W.H.F., Staudigel, H., Watts, A.B. and Pringle, M.S.: The Magellan seamounts: early
1285   Cretaceous record of the South Pacific isotopic and thermal anomaly, J. Geophys. Res., 94,
1286   10501–10523, https://doi.org/10.1029/JB094iB08p10501, 1989.

1287 Staudigel, H. and Hart, S.R.: Alteration of basaltic glass: processes and significance for the oceanic
1288   crust-sewater budget, Geochim. Cosmochim. Acta., 47, 337–350,
1289   https://doi.org/10.1016/0016-7037(83)90257-0, 1983.

1290 Staudigel, H., Park, K.H., Pringle, M., Rubenstone, J.L., Smith, W.H.F. and Zindler, A.: The
1291   longevity of the South-Pacific isotopic and thermal anomaly, Earth Planet. Sci. Lett., 102,
1292   24–44, https://doi.org/10.1016/0012-821X(91)90015-A, 1991.

1293 Stixrude, L. and Lithgow-Bertelloni, C.: Thermodynamics of mantle minerals — I. Physical
1294   properties, Geophys. J. Int., 162, 610–632, https://doi.org/10.1111/j.1365-
1295   246X.2005.02642.x, 2005.

1296 Stoenner, R.W., Schaeffer, O.A. and Katcoff, S.: Half-lives of argon-37, argon-39, and argon-42,
1297   Science, 148, 1325–1328, https://doi.org/10.1126/science.148.3675.1325, 1965.

1298 Stracke, A., Michael, W., Felix, G., Paul, B. and Erin, T.: Major and trace element concentrations and
1299   Sr, Nd, Hf, Pb isotope ratios of global mid ocean ridge and ocean island basalts, GRO data,
1300   V1, https://doi.org/10.25625/0SVW6S, 2022.

1301 Sun, S.-S. and McDonough, W.F.: Chemical and isotopic systematics of oceanic basalts: implications
1302   for mantle composition and processes, Geol. Soc. Spec. Publ., 42, 313–345,
1303   https://doi.org/10.1144/GSL.SP.1989.042.01.19, 1989.

1304 Takahashi, E.: Origin of basaltic magmas: Implications from peridotite melting experiments and an
1305   olivine fractionation model (in Japanese with English abstract), Bull. Volcanol. Soc. Jpn.,
1306   2nd Ser, 30, S17–S40, https://doi.org/10.18940/kazanc.30.TOKUBE_S17, 1986.

1307 Takahashi, E., Uto, K. and Schilling, J.-G.: Primary magma compositions and Mg/Fe ratios of their
1308   mantle residues along Mid Atlantic Ridge 29° N to 73°N, Technical Report of ISEI
1309   Okayama University Series A, 9, 1–4, 1987.

1310 Tamura, A., Arai, S., Takeuchi, M., Miura, M. and Pirnia, T.: Compositional heterogeneity of a
1311   websterite xenolith from Kurose, southwest Japan: insights into the evolution of lower crust
1312   beneath the Japan Arc, Eur. J. Mineral., 31, 35–47, https://doi.org/10.1127/ejm/2018/0030-
1313   2803, 2019.

1314 Taneja, R., Rushmer, T., Blichert-Toft, J., Turner, S. and O'Neill, C.: Mantle heterogeneities beneath
1315   the Northeast Indian Ocean as sampled by intra-plate volcanism at Christmas Island, Lithos,
1316   262, 561–575, http://dx.doi.org/10.1016/j.lithos.2016.07.027, 2016.

1317 Tanimizu, M. and Ishikawa, T.: Development of rapid and precise Pb isotope analytical techniques
1318   using MC-ICPMS and new results for GSJ rock reference samples, Geochem. J., 40, 121–
1319   133. https://doi.org/10.2343/geochemj.40.121, 2006.

1320 Tatsumi, Y., Sakuyama, M., Fukuyama, H. and Kushiro, I.: Generation of arc basalt magmas and
1321   thermal structure of the mantle wedge in subduction zones, J. Geophys. Res., 88, 5815–
1322   5825, https://doi.org/10.1029/JB088iB07p05815, 1983.

1323 Tivey, M.A., Sager, W.W., Lee, S.-M. and Tominaga, M.: Origin of the Pacific Jurassic quiet zone,
1324   Geology, 34, 789–792, https://doi.org/10.1130/G22894.1, 2006.

1325 Uenzelmann-Neben, G., Schmidt, D.N., Niessen, F. and Stein, R.: Intraplate volcanism off South
1326   Greenland: caused by glacial rebound?, Geophys. J. Int., 190, 1–7,
1327   https://doi.org/10.1111/j.1365-246X.2012.05468.x, 2012.

1328 Valentine, G.A. and Hirano, N.: Mechanisms of low-flux intraplate volcanic fields—Basin and
1329   Range (North America) and northwest Pacific Ocean, Geology, 38, 55–58,
1330   https://doi.org/10.1130/G30427.1, 2010.

1331 Walter, M.J.: Melting of garnet peridotite and the origin of komatiite and depleted lithosphere, J.
1332   Petrol., 39, 29–60, https://doi.org/10.1093/petroj/39.1.29, 1998.

1333 Wakaki, S., Shibata, S.-N. and Tanaka, T.: Isotope ratio measurements of trace Nd by the total
1334   evaporation normalization (TEN) method in thermal ionization mass spectrometry, Int. J.
1335   Mass Spectrom., 264, 157–163, http://dx.doi.org/10.1016/j.ijms.2007.04.006, 2007.

1336 Wang, D., Mookherjee, M., Xu Y. and Karato, S.-I.: The effect of water on the electrical conductivity
1337   of olivine, Nature, 443, 977–980, https://doi.org/10.1038/nature05256, 2006.

1338 Wang, X.-J., Chen, L.-H., Hofmann, A.W., Hanyu, T., Kawabata, H., Zhong, Y., Xie, L.-W., Shi, J.-
1339   H., Miyazaki, T., Hirata, Y., Takahashi, T., Senda, R., Chang, O., Vaglarov, B.S. and Kimura,
1340   J.-I. Recycled ancient ghost carbonate in the Pitcairn mantle plume, PNAS, 115, 8682–8687,
1341   https://doi.org/10.1073/pnas.1719570115, 2018.

1342 Weis, D. and Frey, F.A.: Isotope geochemistry of the Ninetyeast Ridge basement basalts: Sr, Nd, and
1343   Pb evidence for involvement of the Kerguelen hot spot, Proc. Ocean Drill. Program Sci.
1344   Results, 121, 591–610, 1991.

1345 Weis, D. and Frey, F.A.: Role of the Kerguelen Plume in generating the eastern Indian Ocean
1346   seafloor. J. Geophys. Res., 101, 13381–13849, https://doi.org/10.1029/96JB00410, 1996.

1347 Weis, D., Kieffer, B., Maerschalk, C., Barling, J., de Jong, J., Williams, G.A., Hanano, D., Pretorius,
1348   W., Mattielli, N., Scoates, J.S., Goolaerts, A., Friedman, R. M. and Mahoney, J.B.: High-
1349   precision isotopic characterization of USGS reference materials by TIMS and MC-ICP-MS,
1350   Geochem. Geophys. Geosyst., 7, Q08006, http://dx.doi.org/10.1029/2006GC001283, 2006.

1351 Weiss, Y., Class, C., Goldstein, S.L. and Hanyu, T.: Key new pieces of the HIMU puzzle from
1352   olivines and diamond inclusions, Nature, 537, 666–670,

https://doi.org/10.1038/nature19113, 2016.

Wessel, P., Luis, J.F., Uieda, L., Scharroo, R., Wobbe, F., Smith, W.H.F., and Tian, D.: The Generic Mapping Tools version 6, Geochem Geophys Geosyst., 20, 5556–5564, https://doi.org/10.1029/2019GC008515. 2019.

Workman, R.K., Hart, S.R., Jackson, M., Regelous, M., Farley, K.A., Blusztajn, J., Kurz, M. and Staudigel, H.: Recycled metasomatized lithosphere as the origin of the Enriched Mantle II (EM2) end-member: Evidence from the Samoan Volcanic Chain, Geochem. Geophys. Geosyst., 5, Q04008, https://doi.org/10.1029/2003GC000623, 2004.

Yamamoto, J., Hirano, N., Abe, N. and Hanyu, T.: Noble gas isotopic compositions of mantle xenoliths from northwestern Pacific lithosphere, Chem. Geol., 268, 313–323, https://doi.org/10.1016/j.chemgeo.2009.09.009, 2009.

Yamamoto, J., Korenaga, J., Hirano, N. and Kagi, H.: Melt-rich lithosphere-asthenosphere boundary inferred from petit-spot volcanoes, Geology, 42, 967–970, https://doi.org/10.1130/G35944.1, 2014.

Yamamoto, J., Kawano, T., Takahata, N. and Sano, Y.: Noble gas and carbon isotopic compositions of petit-spot lavas from southeast of Marcus Island. Earth Planet. Sci. Lett., 497, 139–148, https://doi.org/10.1016/j.epsl.2018.06.020, 2018.

Yamamoto, J., Hirano, N. and Kurz, M.D.: Noble gas isotopic compositions of seamount lavas from the central Chile trench: Implications for petit-spot volcanism and the lithosphere asthenosphere boundary, Earth Planet. Sci. Lett., 552, 116611, https://doi.org/10.1016/j.epsl.2020.116611, 2020.

Yamazaki, S., Neo, N. and Miyashita, S.: Data report: whole–rock major and trace elements and mineral compositions of the sheeted dike–gabbro transition in ODP Hole 1256D, In Teagle, D. A. H., Alt, J. C., Umino, S., Miyashita, S., Banerjee, N. R., Wilson, D. S. and the Expedition 309/312 Scientists (Eds.), Proceedings Integrated Ocean Drilling Program. 309/312: Washington, DC (Integrated Ocean Drilling Program Management International, Inc.) https://doi.org/10.2204/iodp.proc.309312.203.2009, 2009.

Yang, H.-J., Frey, F.A. and Clague, D.A.: Constraints on the Source Components of Lavas Forming the Hawaiian North Arch and Honolulu Volcanics, J. Petrol., 44, 603–627, https://doi.org/10.1093/petrology/44.4.603, 2003.

Yoshino, T., Matsuzaki, T., Yamashita, S. and Katsura T.: Hydrous olivine unable to account for conductivity anomaly at the top of the asthenosphere, Nature, 443, 973–976, https://doi.org/10.1038/nature05223, 2006.

Zakharov, D.O., Tanaka, R., Butterfield, D.A. and Nakamura, E.: A New Insight Into Seawater-Basalt Exchange Reactions Based on Combined $\delta^{18}O$—$\Delta'^{17}O$—$^{87}Sr/^{86}Sr$ Values of Hydrothermal Fluids From the Axial Seamount Volcano, Pacific Ocean. Front. Earth Sci., 9,

691699, https://doi.org/10.3389/feart.2021.691699, 2021.

Zhang, F., Lin, J. and Zhan, W.: Variations in oceanic plate bending along the Mariana trench. Earth Planet. Sci. Lett., 401, 206–214, http://dx.doi.org/10.1016/j.epsl.2014.05.032, 2014.

Zhang, G.L., Chen, L.H., Jackson, M. and Hofmann, A.W.: Evolution of carbonated melt to alkali basalt in the South China Sea, Nat. Geosci., 10, 229–235, https://doi.org/10.1038/ngeo2877, 2017.

Zhang, W., Johnston, S. and Currie, C.A., Kimberlite magmatism induced by west-dipping subduction of the North American plate, Geology, 47, 395–398, https://doi.org/10.1130/G45813.1, 2019.

Zhang, J., Xu, M. and Sun, Z.: Lithospheric flexural modelling of the seaward and trenchward of the subducting oceanic plates, Int. Geol. Rev., 62, 908–923, https://doi.org/10.1080/00206814.2018.1550729, 2020.

Zhang, G., Wang, S., Huang, S., Zhan, M. and Yao, J.: CO_2-rich rejuvenated stage lavas on Hawaiian Islands, Geochem. Geophys. Geosyst., 23, e2022GC010525, https://doi.org/10.1029/2022GC010525, 2022.

Zhong, Y., Zhang, G.-L., Zhong, L.-F., Chen, L.-H. and Wang, X.-J.: Post-spreading volcanism triggered by CO_2 along the South China Sea fossil spreading axis, Lithos, 404–405, 106478, https://doi.org/10.1016/j.lithos.2021.106478, 2021.

Zindler, A. and Hart, S.: Chemical geodynamics, Ann. Rev. Earth Planet. Sci., 14, 493–571, https://doi.org/10.1146/annurev.ea.14.050186.002425, 1986.